

The temporal brightening of Uranus' northern polar hood from HST/WFC3 & HST/STIS observations

Arjuna James¹, Patrick G. J. Irwin¹, Jack Dobinson¹, Michael H. Wong², Troy K. Tsubota², Amy A. Simon³, Leigh N. Fletcher⁴, Michael T. Roman⁴, Nick A. Teanby⁵, Daniel Toledo⁶ and Glenn S. Orton⁷.

¹Department of Physics, University of Oxford, Oxford, UK

²Center for Integrative Planetary Science, University of California, Berkeley, CA, USA

³NASA Goddard Space Flight Center Solar System Exploration Division, Greenbelt, MD, USA

⁴School of Physics and Astronomy, University of Leicester, University Road, Leicester, UK

⁵School of Earth Sciences, University of Bristol, Wills Memorial Building, Queens Road, Bristol, UK

⁶Instituto Nacional de Técnica Aeroespacial, Madrid, Spain

⁷Jet Propulsion Laboratory, California Institute of Technology, Pasadena, CA, USA

Key Points:

- We confirm that the brightening of Uranus' north polar hood is predominantly due to changes in aerosol scattering
- A temporal thickening and increase in aerosol reflectivity of Irwin et al. (2023)'s 1 – 2 bar haze is the main cause of the brightening
- We find a further reduction in polar cloud-top methane over time from retrievals carried out on HST/STIS observations

Corresponding author: Arjuna James, arjuna.james@physics.ox.ac.uk

Abstract

Hubble Space Telescope Wide-Field Camera 3 (HST/WFC3) observations spanning 2015 to 2021 confirm a brightening of Uranus' north polar hood feature with time. The vertical aerosol model of Irwin et al. (2023) (IRW23), consisting of a deep haze layer based at ~ 5 bar, a 1 – 2 bar haze layer, and an extended haze rising up from the 1 – 2 bar layer, was applied to retrievals on HST Space Telescope Imaging Spectrograph (HST/STIS) observations (Sromovsky et al., 2014, 2019) revealing a reduction in cloud-top CH_4 by an average of $0.19 \pm 0.03\%$ between $40 - 80^\circ\text{N}$ between 2012 and 2015. A combination of latitudinal retrievals on the HST/WFC3 & HST/STIS datasets, again employing the IRW23 model, reveal a temporal thickening of the 1 – 2 bar haze layer to be the main cause of the polar hood brightening, finding an average increase of 1.09 ± 0.08 at $0.8 \mu\text{m}$ north of $\sim 45^\circ\text{N}$, concurrent with a decrease in the imaginary refractive index spectrum of the 1 – 2 bar haze layer north of $\sim 40^\circ\text{N}$ and longwards of $\sim 0.7 \mu\text{m}$, and between 60°N and 80°N at $\sim 0.5 \mu\text{m}$. Small contributions to the brightening were found from a thickening of the deep aerosol layer, with an average increase in integrated opacity of 0.6 ± 0.1 north of 45°N between 2012 and 2015, and from the aforementioned decrease in cloud-top CH_4 abundance. Our results are consistent with the slowing of a meridional circulation, exhibiting strong subsidence at the poles.

Plain Language Summary

Uranus' north polar hood - a bright cap-like feature encircling the northern polar region within its atmosphere - is observed to be brightening over time. Using several observations of Uranus captured between 2012 and 2021 by the Hubble Space Telescope, this study aims to pinpoint, for the first time, the specific changes occurring within the atmosphere leading to this evolution. Analysis of the observations confirmed the predominant cause of the hood's brightening as changes in the scattering properties of the atmosphere's aerosol layers. The vertical aerosol model of Irwin et al. (2023) (IRW23), consisting of a deep haze layer based at ~ 5 bar, a 1 – 2 bar haze layer, and an extended haze rising up from the 1 – 2 bar haze layer, was employed to investigate these aerosol layer changes. We find that the hood's brightening mainly stems from changes in IRW23's 1 – 2 bar haze layer, finding a thickening of the layer concurrent with an increase in aerosol reflectivity of with time at latitudes coincident with the north polar hood ($\sim 45 - 90^\circ\text{N}$). Small contributions to the temporal brightening were also found from a $\sim 10\%$ reduction in cloud-top methane and a thickening of IRW23's deep aerosol layer at north polar hood latitudes.

1 Introduction

Uranus' large axial tilt ($\sim 98^\circ$) drives the most extreme solar forcing experienced by any planetary atmosphere in our solar system, leading to seasonal changes in the cloud and haze layers present. The past two decades of observation of the Uranian atmosphere have revealed several discrete features at various locations and epochs, for example, a dark spot, small-scale convective clouds, and convective storm systems (e.g., Irwin et al. (2007); Sromovsky and Fry (2007); Irwin et al. (2009); Hammel et al. (2009); Sromovsky et al. (2009); Irwin et al. (2011, 2017)). In addition to these, one large-scale latitudinal feature observed in the atmosphere is Uranus' so-called polar 'hood', a bright cap-like region encircling the pole and terminating abruptly in the mid-latitudes. The hood was first observed in the visible/near-infrared in the southern hemisphere (Sromovsky & Fry, 2007; Karkoschka & Tomasko, 2009) prior to northern spring equinox (2007), shrouding the polar region at latitudes south of $\sim 45^\circ\text{S}$. The dissipation of this south polar hood into a circumpolar collar (at $\sim 45^\circ\text{S}$) was observed through the equinox. The collar was then seen to reduce in brightness, eventually vanishing, with an almost identical circumpolar collar appearing in the north (at $\sim 45^\circ\text{N}$), eventually evolving into a polar hood

north of $\sim 45^\circ\text{N}$ latitude (Irwin et al., 2007; Sromovsky & Fry, 2007; Irwin et al., 2009, 2012; Sromovsky et al., 2014).

Observations following this period have confirmed the continued presence of the north polar hood, captured with the Hubble Space Telescope’s (HST) Space Telescope Imaging Spectrograph (STIS) (Sromovsky et al., 2014) & Wide-Field Camera 3 (WFC3) (Irwin et al., 2017) instruments, and the Very Large Telescope’s (VLT) Spectrograph for Integral Field Observations in the Near Infrared (SINFONI) (Toledo et al., 2018). Karkoschka and Tomasko (2009), using HST/STIS observations of Uranus, revealed latitudinal variability in the cloud-top methane (CH_4) abundance, decreasing by a factor of ~ 2.3 from the equator to the pole in the southern hemisphere. Sromovsky et al. (2014) then confirmed the existence of this cloud-top CH_4 abundance gradient in the northern hemisphere from 2012 HST/STIS observations, and furthermore, that observations implied that the southern and northern cloud-top CH_4 depletions were simultaneously present during northern spring equinox in 2007. It was concluded that the polar depletions are likely a persistent feature of Uranus’ atmosphere.

This motivated Toledo et al. (2018) to probe CH_4 depletion as a possible source of the bright appearance of the polar hood. Their results concluded that the depletion in polar cloud-top CH_4 volume mixing ratio (VMR) was responsible for the hood’s bright appearance, as opposed to latitudinal variations in the optical properties or abundance of aerosols. Later observations of Uranus obtained with HST/STIS in 2015 (Sromovsky et al., 2019) enabled a window into the temporal evolution of the hood by comparison with previous observations from 2012 (Sromovsky et al., 2014). An apparent brightening of the north polar hood with time was detailed by Sromovsky et al. (2019) who performed a retrieval study that concluded that the change was driven by increased aerosol scattering. Sromovsky et al. (2019) acknowledged that the persistent polar depletion in upper tropospheric CH_4 aids in the brighter appearance of the north polar hood, in agreement with Toledo et al. (2018). However, it was concluded that this depletion cannot account for the temporal change observed due to its spectral signature including wavelengths dominated by hydrogen absorption and due to the polar depletion in CH_4 VMR being found to be ‘generally stable’ between the two observations. Toledo et al. (2019) subsequently carried out microphysical simulations to constrain the formation and structure of haze in Uranus’ atmosphere, revealing timescales for haze particles to grow and settle out to be $\gtrsim 30$ years at pressure levels > 0.1 bar. This is too long to explain the observed variations in the haze structure over Uranus’ northern hemisphere post-equinox, hinting at a dynamical origin of the spatial and temporal distribution of the haze over the poles. To date, no study has managed to pinpoint the exact aerosol layer change(s) involved in the brightening of the polar hood within a chosen vertical aerosol model, which is what this study intends to address.

Irwin et al. (2022), using an array of data sourced from HST/STIS, HST/WFC3, the Infrared Telescope Facility’s SpeX (IRTF/SpeX) instrument (a medium resolution spectrograph) and Gemini-North’s Near-Infrared Integral-Field Spectrograph (Gemini/NIFS), were able to produce an holistic vertical aerosol model simultaneously fitting these datasets for both ice giant atmospheres (i.e., Uranus & Neptune). The model consists of three layers (outlined in full in Section 2.3): a deep layer assumed to be composed of a mixture of H_2S ice and photochemical haze, a layer of photochemical haze/ice at the methane condensation level, and an extended layer of photochemical haze extending from this level up through to the stratosphere. This holistic model was then improved upon by Irwin et al. (2023) by modifying the deep aerosol layer to be a compact layer based at ~ 5 bar as opposed to the original diffuse layer.

We employ the HST/STIS observations from 2012 (Sromovsky et al., 2014) & 2015 (Sromovsky et al., 2019) in this investigation, in addition to yearly observations of Uranus spanning 2015 – 2021 obtained from the Outer Planetary Atmospheres Legacy (OPAL) programme using HST/WFC3. We use the NEMESIS radiative transfer retrieval code

(Irwin et al., 2008), combined with the modified version of the holistic ice giant aerosol model produced by Irwin et al. (2023), to probe the north polar hood brightening and identify its origin within this vertical aerosol scheme. The Minnaert limb-darkening approximation, which has previously been demonstrated to considerably improve latitudinal CH₄ profile determinations on Neptune (Irwin et al., 2021), is also utilised. We give a full description of the observations used in the investigation, followed by an outline of the aerosol model of Irwin et al. (2023) in Section 2. The results of a Minnaert limb-darkening analysis of the HST/WFC3 dataset, and results from retrievals carried out on the HST/WFC3 & HST/STIS datasets, are then presented in Section 3. A discussion of the results follows in Section 4 with plausible mechanisms explored. Finally a summary of our results, along with our conclusions, are given in Section 5.

2 Observations & aerosol model

2.1 HST/WFC3

Observations of Uranus were obtained using Hubble Space Telescope’s (HST) Wide Field Camera 3 (WFC3) instrument in seven different spectral bands defined by WFC3’s UVIS medium-band and narrow-band filters, displayed in Fig. 1 and Table 1.

Table 1. The seven HST/WFC3 filters used by the Outer Planet Atmospheres Legacy programme to obtain the observations of Uranus used in this study.

Name (Aperture)	λ_0 (nm)	FWHM (nm)
F467M (UVIS)	467	21.5
F547M (UVIS)	547	70.9
FQ619N (UVIS)	619	6.1
F657N (UVIS)	657	12.1
FQ727N (UVIS2)	727	6.4
F763M (UVIS)	763	70.9
F845M (UVIS)	845	87.6

The observations span 2015 – 2021, each taken ~ 1 year apart during 8 HST orbits and covering two full rotations of Uranus. Images were navigated using an ellipsoid limb-fitting technique with equatorial and polar radii of 25,559 and 24,973 km, respectively. The FQ727N data were fringe corrected post-pipeline, resulting in a $\sim 1.1\%$ correction. Data were re-calibrated in accordance with the latest WFC3 calibration pipeline (calwf3 3.6.2), accounting for time-dependent sensitivity changes, resulting in a $\sim 0.3 - 0.8\%$ correction (dependent on the filter and epoch) <https://github.com/spacetelescope/hstcal/releases>. Images in each filter were selected in which discrete storms and clouds were absent. This was decided in order to avoid such bright discrete features from skewing our Minnaert latitudinal analyses. The precise observations used in the analysis are available on the MAST archive at <http://dx.doi.org/10.17909/det7-s122>.

Fig. 2 displays the images from each WFC3 filter for the 2015 and 2021 datasets used. The progress of Uranus’ orbit towards northern summer solstice (occurring in 2030) can be seen via the north polar hood swinging further into view as seen from the Earth.

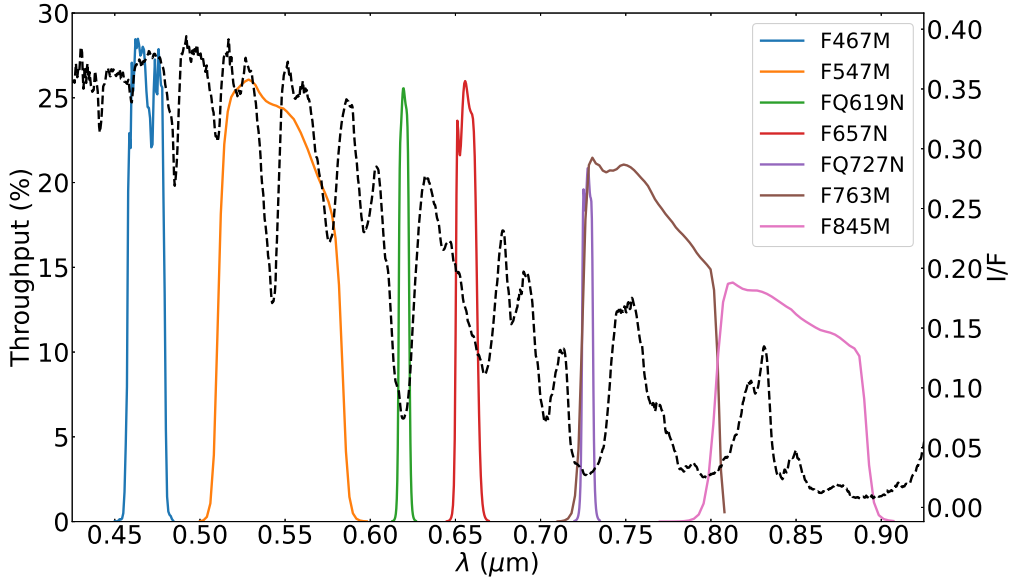


Figure 1. The seven HST/WFC3 filters used for 2015 – 2021 observations of Uranus on a plot of throughput against wavelength in microns. The dashed grey line displays the disc-averaged reflectivity (I/F) spectrum of the 2015 HST/STIS cube as a reference for the spectral features captured by each filter.

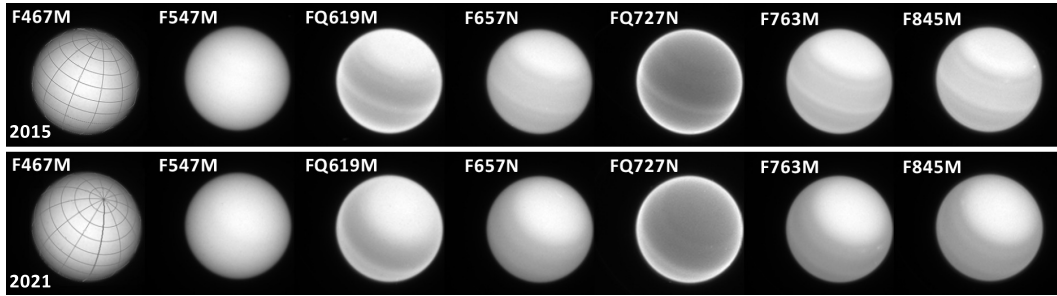


Figure 2. HST/WFC3 images in each of the seven filters for the 2015 (top) and 2021 (bottom) datasets. The 0.467- μm images include superimposed latitude-longitude grids with spacing of 30° between all lines. The north pole (at upper right of disc) is seen to swing further into view over the 6-year timespan between the two sets of observations as Uranus approaches northern summer solstice in 2030.

153

2.2 HST/STIS

154

155

156

157

158

159

160

161

162

Observations of Uranus using the Space Telescope Imaging Spectrograph instrument on HST were both made using four HST orbits, taken on 27 – 28 September 2012 (2012-09-27-21:38:11 – 2012-09-28-01:15:31 UT) (Sromovsky et al., 2014) and 10 October 2015 (14:09:48 – 17:44:54 UT) (Sromovsky et al., 2019). Two of STIS’s gratings, the G430L grating covering 290 – 570 nm with a 0.273 nm/pixel dispersion, and the G750L grating covering 524 – 1027 nm with a 0.492 nm/pixel dispersion, were utilised. HST/STIS is a long-slit spectrometer, but the $51'' \times 0.10''$ long-slit was aligned with the planet’s polar axis and stepped across the disc at intervals of $0.152''$ from centre to edge for the G430L grating (because the planet has no high spatial resolution center-to-limb features

at these wavelengths, interpolation was used to fill in the missing columns of the mosaic), and stepped by $0.0562''$ intervals for the G750L grating, forming a “cube” of half the planet, where at each location on the disc a complete spectrum covering $300.4 - 1,020.0$ nm was recorded at a resolution of 1 nm, sampled every 0.4 nm. We then smoothed the HST/STIS observations to IRTF/SpeX

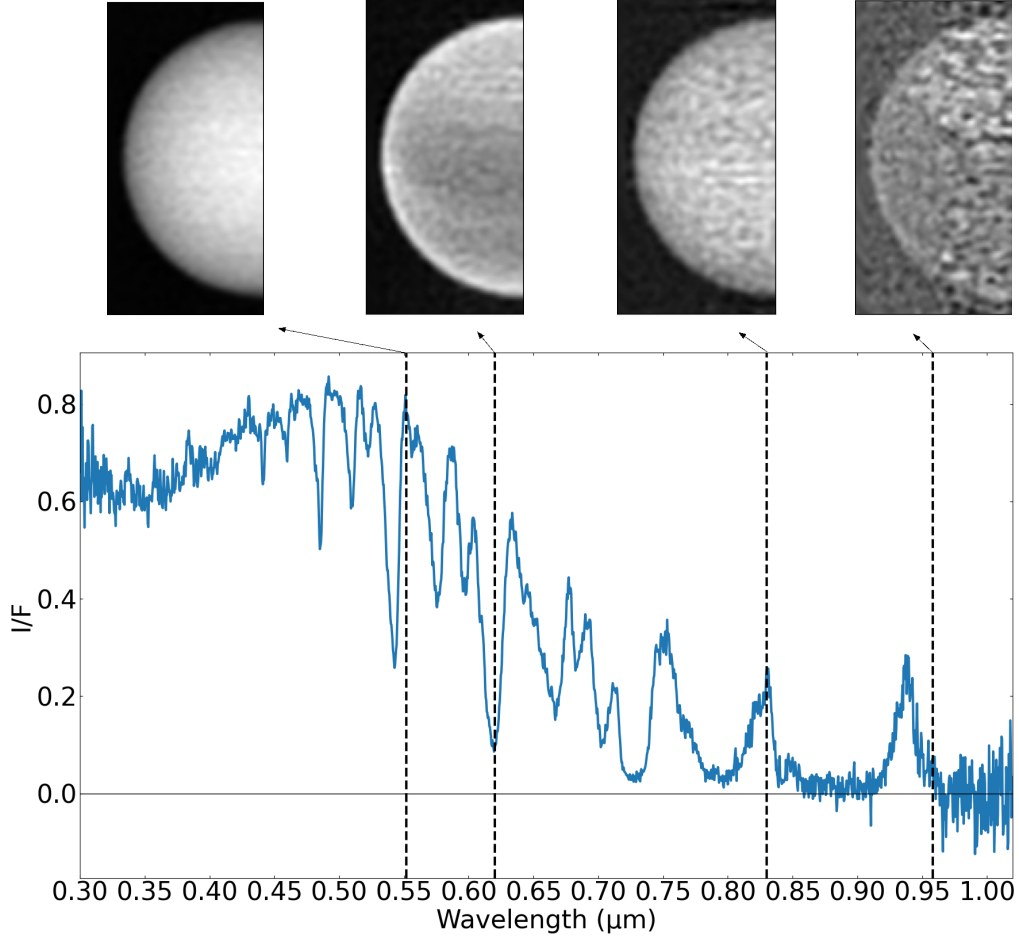


Figure 3. A plot of the reflectivity spectrum extracted from a point at the centre of the disc of our 2015 HST/STIS observation, demonstrating the significant increase in noise (decrease in signal-to-noise ratio) longwards of $\sim 0.95 \mu\text{m}$. Images at $0.552 \mu\text{m}$, $0.62 \mu\text{m}$, $0.83 \mu\text{m}$ and $0.958 \mu\text{m}$ are shown above to visually demonstrate the increase in noise, covering representative wavelengths from both continuum and methane-absorbing regions.

resolution of 2 nm and sampled on a regular grid of spacing 1 nm. This was due to the CH_4 absorption coefficients being used being at the same resolution as IRTF/SpeX (i.e., resolution of 2 nm) (Karkoschka & Tomasko, 2010), allowing us to achieve more efficient retrieval times after smoothing without losing any true resolution in the data.

It should be noted that for the 2015 cube, an error in the program resulted in half of the half-disc being covered with STIS’s nominal $0.05''$ slit instead. This produced a higher spectral resolution at the cost of a significant reduction in signal to noise ratio. The data were pipeline processed, extracted, calibrated, and combined with the uniform spatial and spectral sampling above, described in Sromovsky et al. (2019).

Uranus rotated more than 45° over the course of these observations, resulting in the assumption of a high degree of zonal symmetry in Uranus' atmosphere being embedded within our analysis from the outset. Finally, it should be noted that the data longward of ~ 950 nm was significantly effected by noise for both observations, demonstrated by the plot and images in Fig. 3. This region of the spectrum was therefore omitted from the analysis to avoid the low signal-to-noise ratio (SNR) skewing our retrieval results.

2.3 Aerosol model

The vertical aerosol distribution model used in this investigation is that of Irwin et al. (2023) (IRW23), an improved iteration of the previous holistic model found by Irwin et al. (2022). This consists of: 1) a deep compact aerosol layer centred at $p \simeq 5$ bar, assumed to be composed of a mixture of H_2S ice and photochemical haze (aerosol-1); 2) a layer of photochemical haze/ice, coincident with a layer of high static stability at the CH_4 condensation level at 1 – 2 bar (aerosol-2); and 3) an extended layer of photochemical haze, likely mostly of the same composition as the 1 – 2-bar layer, extending from this level up through to the stratosphere (aerosol-3) (Irwin et al., 2023). This is displayed in Fig. 4.

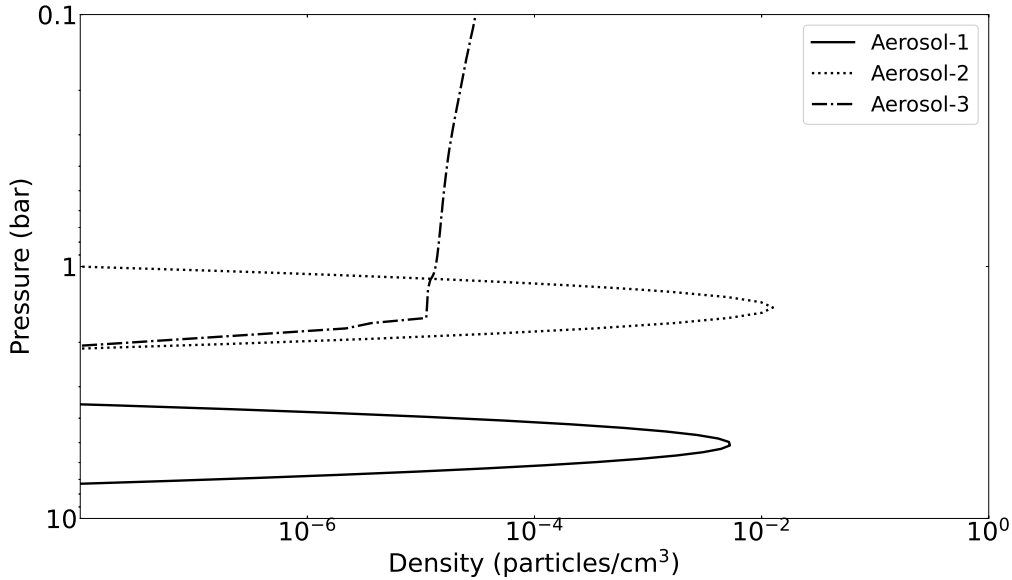


Figure 4. Plot of particle density against pressure retrieved from the disc-averaged HST/STIS 2015 observations using the IRW23 vertical aerosol model.

3 Analysis & results

3.1 Minnaert analysis of HST/WFC3 observations

The Minnaert limb-darkening approximation (Minnaert, 1941) provides an efficient way to model the centre-to-limb variations of a given observation of a planet's full disc. The model approximates the reflectivity, $\frac{I}{F}$, for a given observation at a particular wavelength, taking the form:

$$\frac{I}{F} = \left(\frac{I}{F} \right)_0 \mu_0^k \mu^{k-1} \quad (1)$$

Where $\left(\frac{I}{F} \right)_0$ is the fitted nadir reflectance, k is the fitted limb-darkening parameter and μ & μ_0 are the cosines of the viewing and solar zenith angles, respectively. This model has been successfully vetted for work carried out on VLT/MUSE Jupiter observations (Pérez-Hoyos et al., 2020), and more relevant to our work, on HST/STIS Neptune observations (Irwin et al., 2022) and VLT/MUSE Neptune observations (Irwin et al., 2021) in conjunction with the same NEMESIS radiative transfer retrieval code used in this investigation.

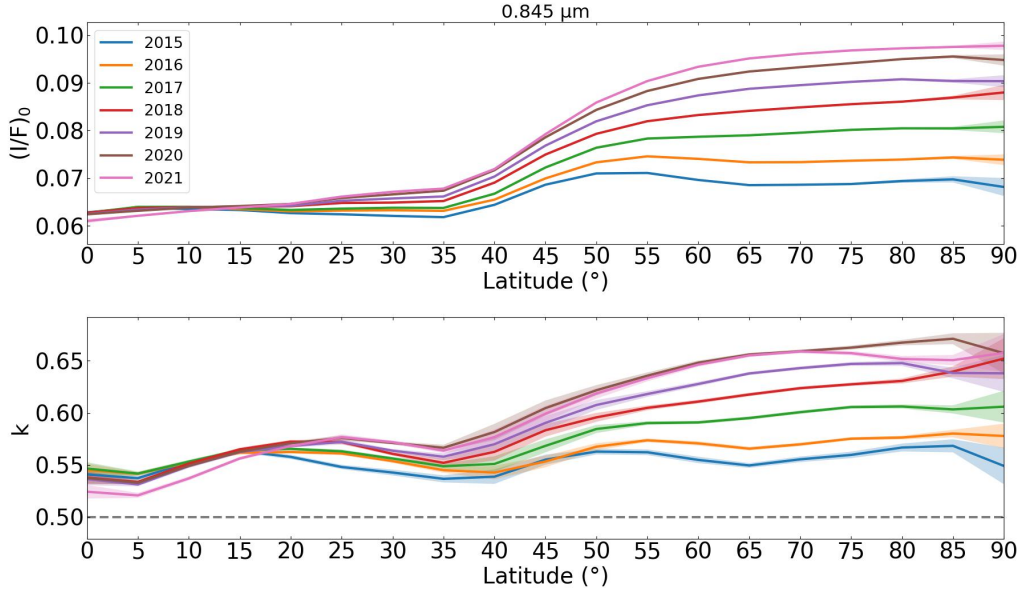


Figure 5. Plot of the fitted Minnaert parameters $\left(\frac{I}{F} \right)_0$ and k versus latitude for the $0.845 \mu\text{m}$ filter observations of our HST/WFC3 dataset of Uranus. A clear trend is observed of a relatively large increase in brightness (i.e., $\left(\frac{I}{F} \right)_0$) north of $\sim 45^\circ\text{N}$ over time. A very similar trend is also observed in the limb-darkening parameter, k . The legend applies to both plots. The black dashed line on the lower plot represents the transition point between limb-darkening ($k > 0.5$) and limb-brightening ($k < 0.5$). Errors are shown to 3σ .

We first applied the approximation to our HST/WFC3 dataset in order to carry out a latitudinal analysis of the fitted Minnaert parameters. The disc was divided into latitude bands of width 10° , stepped across the disc with step size 5° . These latitude bands were then fit to Eqn. 1 individually, fitting profiles for the Minnaert parameters $\frac{I}{F_0}(\phi)$ and $k(\phi)$ as functions of latitude, ϕ , in each of the seven spectral filters. It should be noted that as we move to high northern latitudes, the lack of zenith angle coverage results in the limb of the planet no longer being captured by the latitude bands defined above, meaning the fits of the limb-darkening parameter k are less reliable (cutoff latitude bands centred at 60°N for 2015 and at 35°N for 2021). This increase in uncertainty is incorporated into the latter retrieval work in this paper by a scaling of the measurement errors with latitude, defined in Subsection 3.2. An alternative method to account for the added uncertainty by fixing k to the average value of all latitudes north of the cutoff latitude was attempted, but this did not produce physically plausible results near the north pole.

The motivation behind this initial analysis is the Minnaert approximation’s ability to provide a measure of brightness independent of viewing angle. This appears in the form of the fitted $(\frac{I}{F})_0$ parameter, enabling a direct comparison of the brightness between different regions on the disc. Figs. 5 & 6 show the results for two of the spectral filters, 0.845 μm and 0.727 μm , chosen as representative filters in which the polar hood is distinctly visible and in which it is not visible, respectively (see Fig. 2).

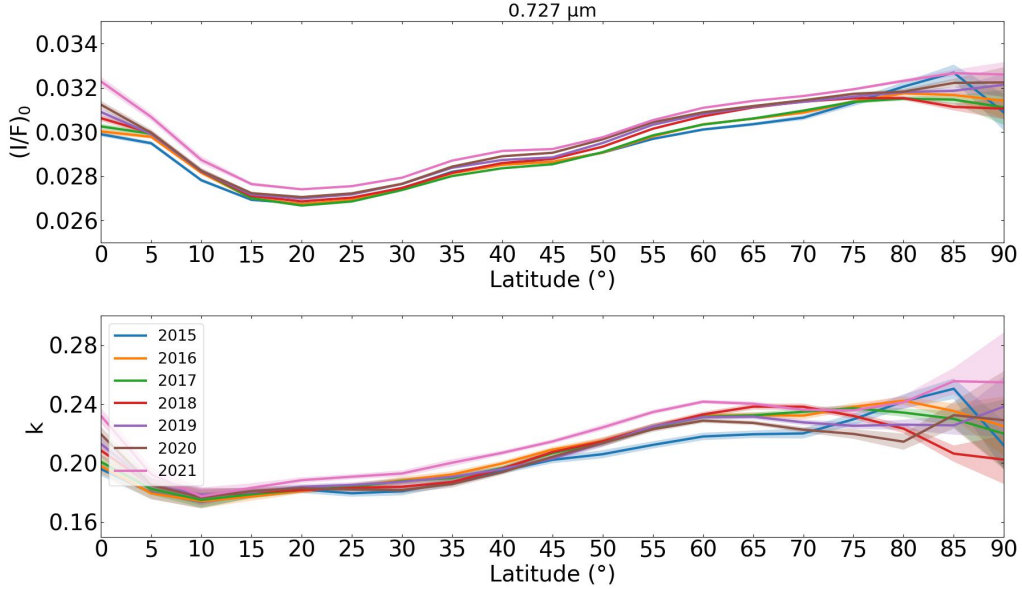


Figure 6. Plot of the fitted Minnaert parameters $(\frac{I}{F})_0$ and k versus latitude for the 0.727 μm filter observations of our HST/WFC3 dataset of Uranus. No clear, simple trend in the Minnaert parameters is observed with time, but an overall small but fairly consistent brightening across latitudes is seen across the entire timespan of the data. The legend applies to both plots. Errors are shown to 3σ .

The latitudinal profiles of the fitted Minnaert parameters correlate very well with the north polar hood. Namely, for wavelengths in which the polar hood is distinctly visible (e.g., 0.845 μm), the observed increase in brightness at northern polar latitudes with time is significantly more pronounced than that of equatorial latitudes or the mid-latitudes (average increase in reflectivity of $\sim 0.0044/\text{year}$ at 65°N compared to $\sim 0.00084/\text{year}$ at 30°N , a ~ 5.25 -fold difference), and for wavelengths in which the polar hood cannot be clearly discerned (e.g., 0.727 μm), there is no such asymmetry in the change in brightness in the northern hemisphere, or one of a much lesser degree.

This result is significant insofar as it confirms a ‘true’ brightening of the polar hood, ruling out any apparent brightening effects due to changes in the viewing geometry as significant contributors. This suggests that the main contributors to the polar hood brightening over time must originate from changes in the cloud-top CH_4 VMR and/or changes in the aerosol layers within Uranus’ atmosphere (changes in scattering and/or optical properties). This is reflected by the fact that the 0.727 μm filter probes high up in the troposphere ($\lesssim 1$ bar) and shows no signs of the bright polar hood or its evolution with time, whereas the 0.845 μm , probing pressures of a few bars that coincides with the expected location of the aerosol layers and also the pressure sensitivity to CH_4 VMR, shows a strong signature of the hood and its brightening.

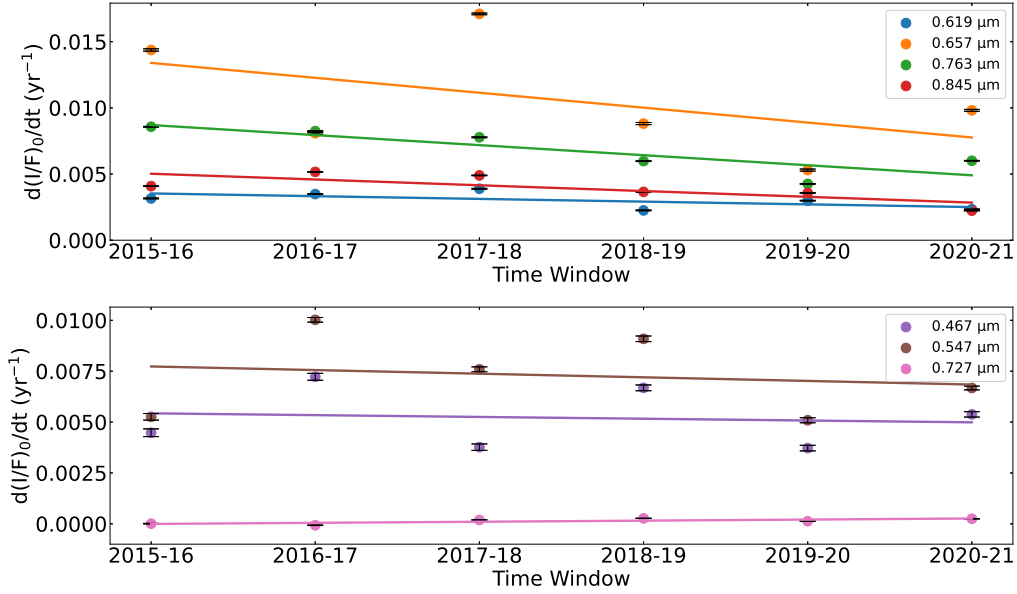


Figure 7. Plots of the average rate of change in brightness (i.e., the rate of change in $(\frac{I}{F})_0$) against the 1-year time window considered. datapoints are calculated from the average change across polar hood latitudes ($45 - 90^\circ\text{N}$) between consecutive years in the HST/WFC3 dataset. Plots are separated by the filters in which the hood is distinctly visible (*top*) and in which it is not (*bottom*) (see Fig. 2). Linear fits to the datapoints from each filter are included. These fits display trends of a decrease in the rate of brightening with time within the hood for the filters in which it is distinctly visible (0.619, 0.657, 0.763 and 0.845 μm), and trends of a virtually constant rate of brightening in comparison for those in which the hood is not (0.467 and 0.727 μm). The 0.547- μm filter does in fact show an increased signature of brightening at polar hood latitudes ($45 - 90^\circ\text{N}$) compared to equatorial & mid-latitudes despite the hood not being clearly visible (see Fig. 2), and shows a trend of a decrease in the rate of brightening over time here.

Fig. 5 also appears to show signs of a decrease in the amount of brightening year on year. To investigate this, we took the average change in brightness (i.e., change in $(\frac{I}{F})_0$) over the polar hood latitudes ($45 - 90^\circ\text{N}$) between successive years for each WFC3 filter and plotted these along with linear fits to observe any potential trends (Fig. 7). We indeed observe a tentative slowing in the rate of brightening for the filters in which the hood is distinctly visible over the timespan of the dataset. This suggests that the change(s) responsible for the polar hood brightening, and the underlying mechanism(s) involved, could be slowing down with time. The filters in which the hood is not visible show tenuous trends by comparison. Note that the 0.547- μm filter (Fig. 7) does in fact show an increased signature of brightening at polar hood latitudes ($45 - 90^\circ\text{N}$) compared to equatorial & mid-latitudes despite the hood not being clearly visible.

3.2 Latitudinal CH_4 profile from HST/STIS observations

Due to the lack of spectral resolution in the HST/WFC3 observations, we cannot directly retrieve the latitudinally-dependent cloud-top CH_4 VMR profile using the method of Karkoschka and Tomasko (2009). This utilises the 818 – 832 nm region of Uranus’ spectrum, which is dominated by hydrogen collision-induced absorption (CIA), to compare to regions dominated by CH_4 absorption, enabling a degeneracy that exists between cloud-

top pressures and the cloud-top CH_4 mixing ratio within retrievals to be broken. Thus, HST/STIS data, possessing a high spectral resolution, were employed in order to probe the temporal stability of the polar depletion in cloud-top CH_4 VMR in an attempt to test the conclusion of Sromovsky et al. (2019), and also to retrieve a latitudinal CH_4 profile to inform our latter retrievals on the HST/WFC3 dataset.

To efficiently model the observed centre-to-limb variations of the HST/STIS observations, we again employed the Minnaert limb-darkening approximation described in Section 3.1. The observations were Minnaert-analysed in latitude bands of width 10° across the disc with a step size of 5° , deriving spectra for $(\frac{I}{F})_0(\lambda)$ and $k(\lambda)$ as functions of wavelength, λ . Uranus is sufficiently distant from the Earth and the Sun such that the solar zenith angle and viewing zenith angle can be approximated to be the same (i.e., $\mu = \mu_0$), simplifying the Minnaert equation to $\frac{I}{F} = (\frac{I}{F})_0 \mu^{2k-1}$. The fitted Minnaert parameters $(\frac{I}{F})_0(\lambda)$ and $k(\lambda)$ were then used to generate reconstructed spectra at two viewing zenith angles (0° , 61.45°), corresponding to two of the five zenith angles of the Gauss-Lobatto multiple-scattering radiative transfer model used within the NEMESIS retrieval code. The higher angle is large enough to ensure that we fully capture the observed limb-darkening (or limb-brightening), and is coincident with one of the Gauss-Lobatto quadrature angles, saving the need for any interpolation (Irwin et al., 2021). These reconstructed spectra were then implemented as a set of “measured” observations to feed into NEMESIS retrievals. Using Eqn. 1, we can reproduce the observations at any other zenith angle, assuming that the Minnaert approximation holds at all other zenith angles in our zenith-angle quadrature scheme, which Irwin et al. (2021) found to be a good approximation for their analysis of VLT/MUSE Neptune observations.

The NEMESIS retrieval code was recently updated to incorporate the effects of Raman scattering and polarisation (Irwin et al., 2022), important for wavelengths $< 0.55 \mu\text{m}$ in Uranus’ atmosphere. To fully capture the effects of these phenomena on reflectivity at the limit of our wavelength range ($0.3 \mu\text{m}$), we extrapolated the reflectivity at $0.3 \mu\text{m}$ down to $0.2 \mu\text{m}$ with a $0.001 \mu\text{m}$ interval (setting each reflectivity value to that at $0.3 \mu\text{m}$). These extrapolated reflectivity values were then multiplied by the solar spectrum at the corresponding wavelength and given very large errors (100%) to prevent NEMESIS from trying to fit to them and skewing our retrievals, whilst simultaneously incorporating effects from Raman scattering and polarisation.

Similar to Irwin et al. (2022), we found that we were able to fit the HST/STIS reflectivity spectra to a precision of reduced- $\chi^2 \sim 1$ if we assumed the errors to be equivalent to $1/50$ of the peak reflectivity in each wavelength bin ($0.1 \mu\text{m}$ bin width with a step size of $0.05 \mu\text{m}$). This estimated error covers unknown systematic uncertainties from sources such as the Lucy-Richardson spatial deconvolution applied to the HST/STIS data, the inhomogeneous aerosol structure, and the methane absorption k -table parameters (Irwin et al., 2022). The spectral fit of the IRW23 model to the Minnaert-reconstructed disc-averaged spectrum is shown in Fig. 8, having a reduced- χ^2 of 1.16.

Retrievals were then carried out on the individual latitude bands over the full wavelength range, with the free parameters in our aerosol model being: aerosol-1 integrated opacity (τ_1), aerosol-2 integrated opacity (τ_2) & base pressure (p_2), aerosol-3 integrated opacity (τ_3) and cloud-top CH_4 VMR. All parameters were given 100% *a priori* errors. The imaginary refractive index spectrum of each layer, defining the reflection/absorption profile of its aerosols with wavelength, was also allowed to vary with 10% *a priori* errors (the real part of the refractive index was set to 1.4 at $0.8 \mu\text{m}$ for each layer).

When carrying out latitudinal analyses on these data, it is important to account for the fact that the viewing angle becomes limited as we move from the middle of the disc towards northern polar latitudes or southern mid-latitudes (due to the orbital phase moving towards northern summer solstice after northern spring equinox in 2007), resulting in reduced constraints on our retrievals and Minnaert fits. We accounted for this re-

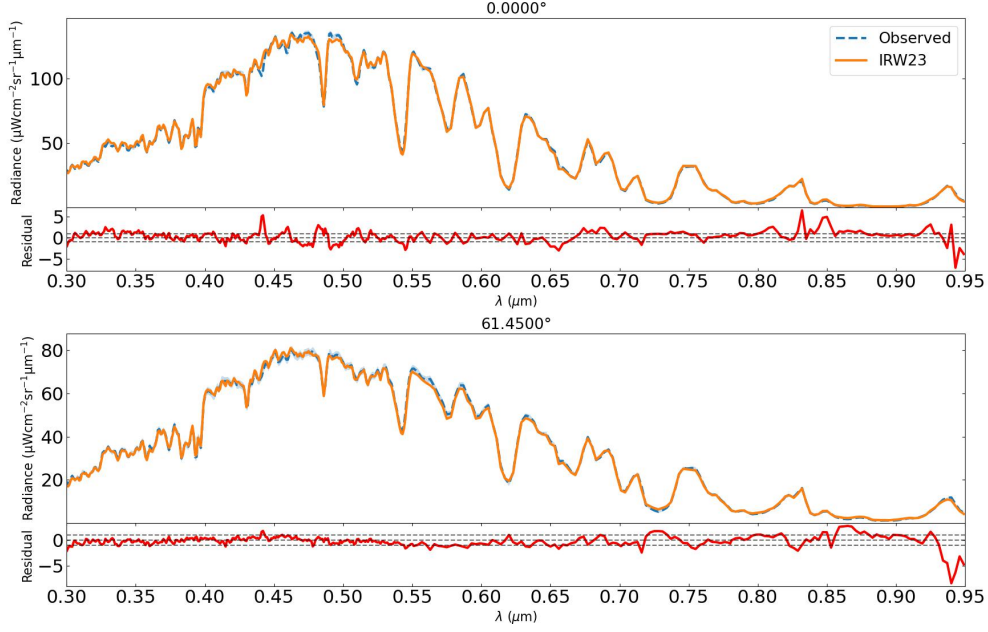


Figure 8. Plot of disc-averaged radiance against wavelength for the 2015 HST/STIS cube at the two chosen Minnaert zenith angles (0° , 61.45°), displaying the spectral fit to the disc-averaged reconstructed Minnaert spectrum of the IRW23 aerosol model. The fit has a reduced- χ^2 value of 1.16. Note, residuals are divided by the error on the measured spectrum.

duction in constraint within the errors extracted from our Minnaert analyses at each visible latitude band for the two datasets. We carried this out by implementing a scaling factor that was applied to the assumed errors described above (1/50 of the peak reflectivity in each wavelength bin). Our yardstick was chosen as the number of datapoints in each latitude band within our Minnaert analysis (i.e., the number of datapoints on the $\mu \frac{I}{F}$ vs $\mu \mu_0$ plot). This scaling factor was normalised such that it is equal to unity for the visible latitude band with the largest number of datapoints, and therefore increases as we move away from the centre of the disc. This scaling factor is defined in Eqn. 2:

$$f_{\phi_{band}} = \sqrt{\frac{n_{max}}{n}} \quad (2)$$

Where $f_{\phi_{band}}$ is the scaling factor ($f_{\phi_{band}} \geq 1$) for a given latitude band ϕ_{band} , n is the number of datapoints in the latitude band being considered, and n_{max} denotes the largest number of datapoints found within a single latitude band across all visible latitude bands.

The resulting spectral fits of these retrievals at representative latitude bands, in the equatorial and polar regions, are shown in Figs. 9 and 10.

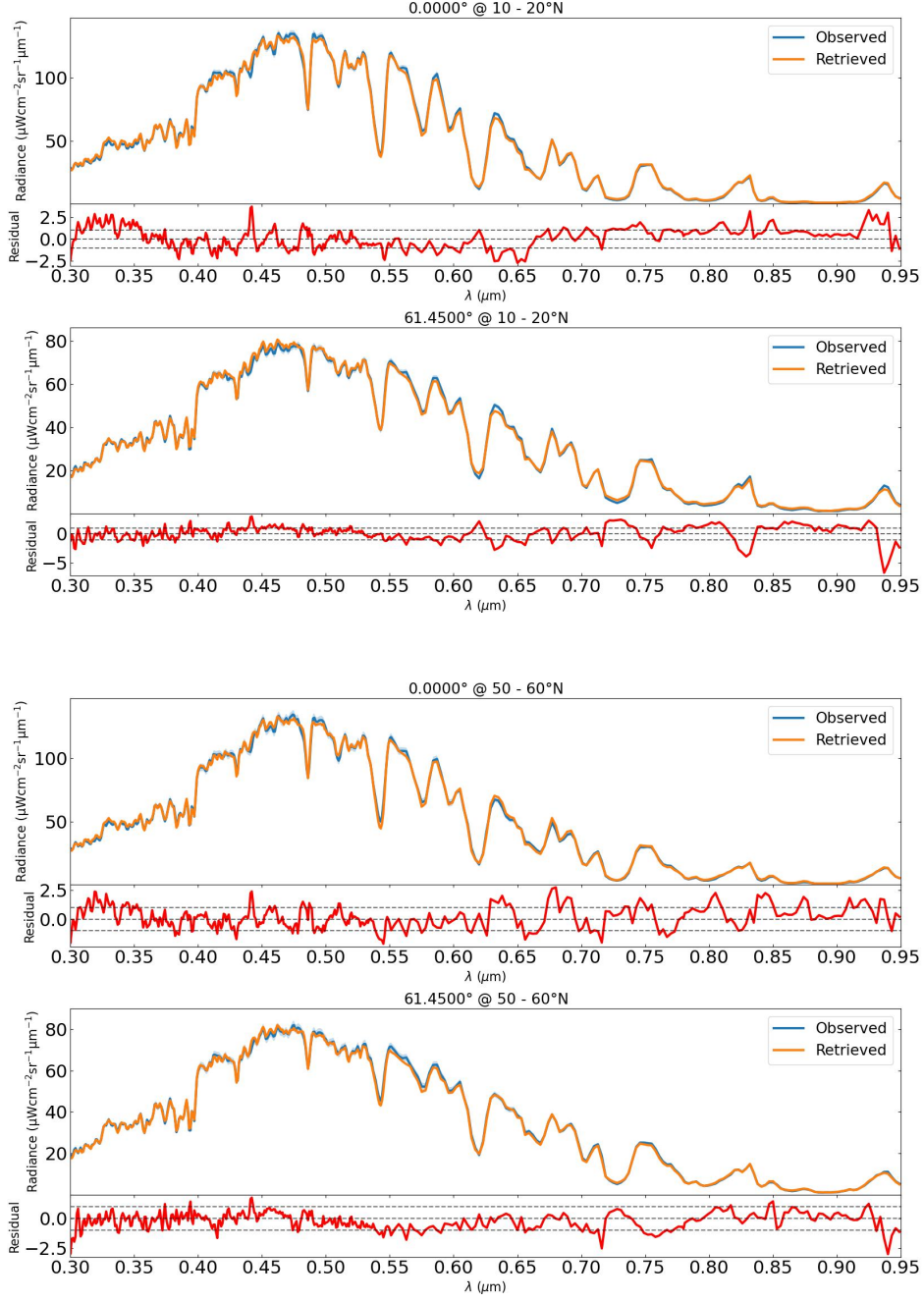


Figure 9. Plots of radiance against wavelength showing the spectral fits at the two chosen Minnaert zenith angles (0° , 61.45°) for retrievals carried out on the 2012 STIS observation at representative latitude bands of 10 – 20°N (top) & 50 – 60°N (bottom). Note, residuals are divided by the error on the measured spectrum.

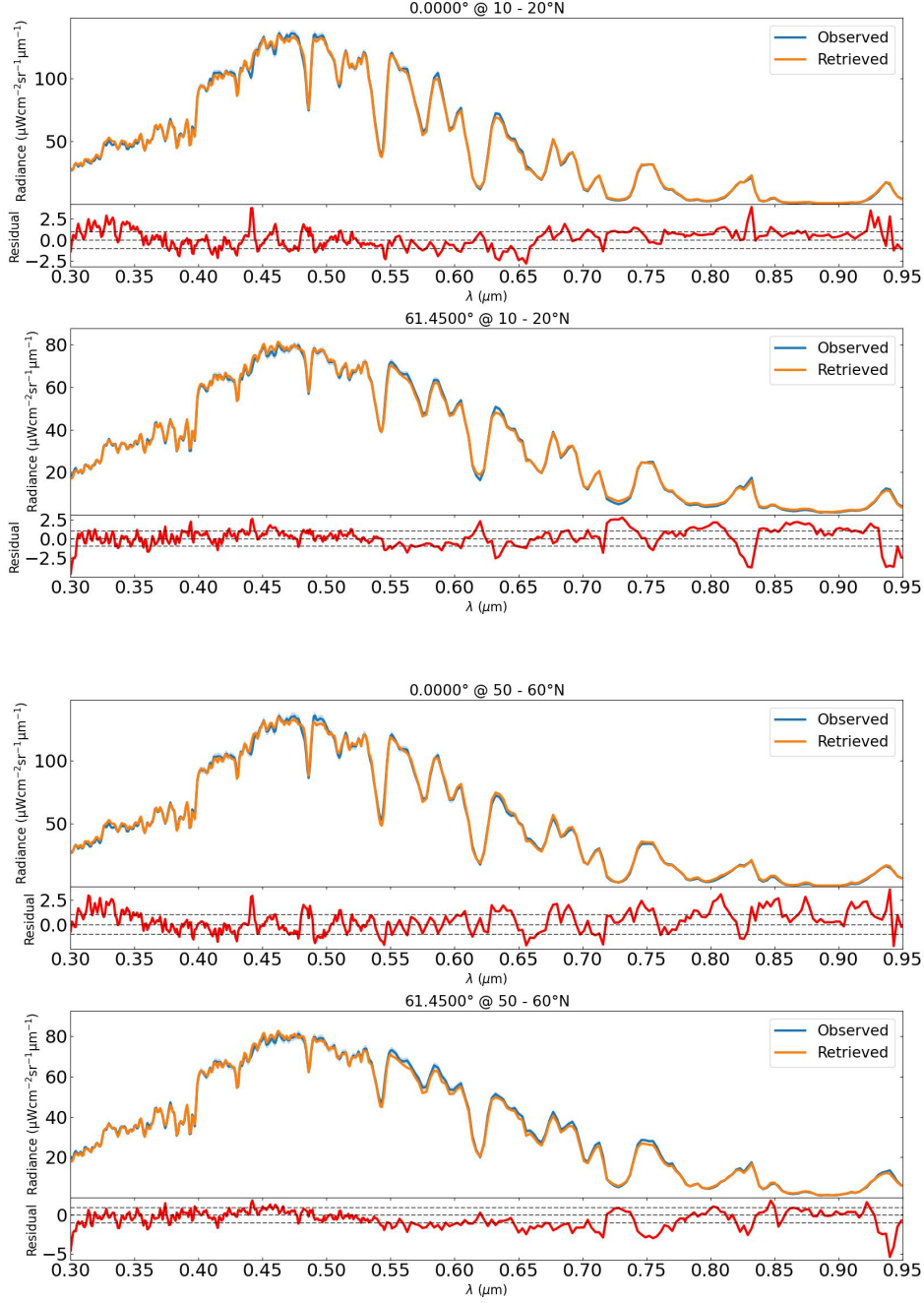


Figure 10. Plots of radiance against wavelength showing the spectral fits at the two chosen Minnaert zenith angles (0° , 61.45°) for retrievals carried out on the 2015 STIS observation at representative latitude bands of 10 – 20°N (top) & 50 – 60°N (bottom). Note, residuals are divided by the error on the measured spectrum.

The resulting retrieved latitudinal profiles of cloud-top CH_4 VMR are displayed in Fig. 11. It can be seen that the retrieved profiles for the two datasets are largely similar. However, a small but distinct reduction in cloud-top CH_4 is observed between $\sim 40^\circ\text{N}$ and 80°N , coinciding with the north polar hood. This suggests that a contributing factor to the temporal brightening between the two observations does indeed originate from a further depletion in polar cloud-top CH_4 with time. However, due to the fact that it

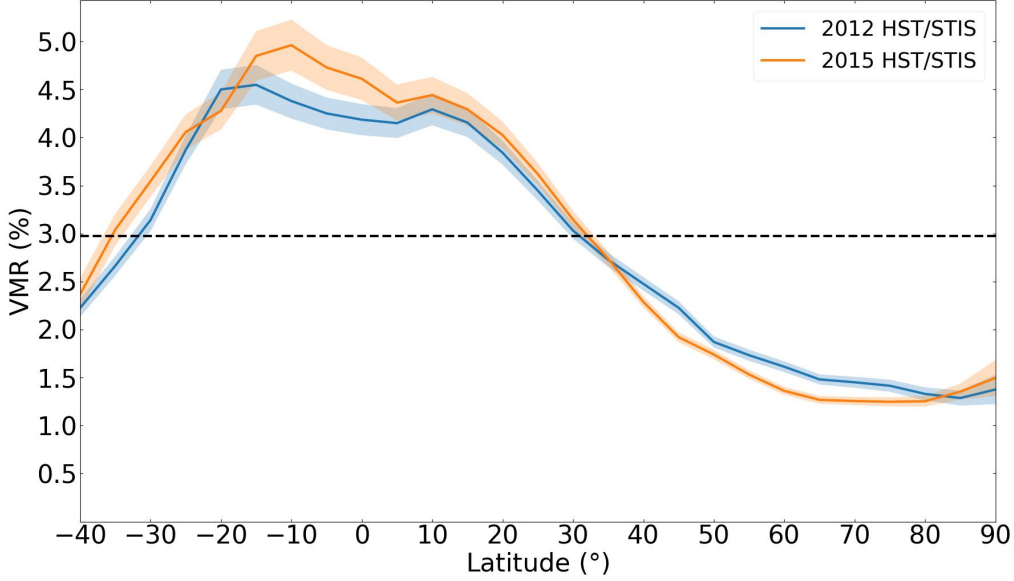


Figure 11. Plot of volume mixing ratio against latitude displaying the latitudinal profiles of the cloud-top CH₄ mixing ratio retrieved from the 2012 & 2015 STIS observations. The two profiles appear largely similar, however, the 2015 profile shows a small reduction in cloud-top CH₄ mixing ratio between $\sim 40 - 80^\circ\text{N}$. The established negative gradient in cloud-top CH₄ mixing ratio when moving from equator to pole is clearly seen. The black dashed line denotes the *a priori* value of 2.97%.

is not entirely clear how the latitudinally-dependent cloud-top CH₄ VMR varies in the northern hemisphere over short (≤ 1 yr) or long timescales (\geq a few years), further observations and retrieval work would be required to confirm whether this is a continued trend over time. It is entirely plausible that there may be interseasonal variability in the cloud-top CH₄ VMR over short or long timescales in this dynamically active region. The conclusion of this depletion being ‘generally stable’ over time by Sromovsky et al. (2019) appears to be a safe and conservative one in light of this. We thus assert that this conclusion holds for the timespan of our HST/WFC3 dataset (2015 – 2021), enabling us to fix the latitudinal cloud-top CH₄ VMR profile for our HST/WFC3 retrievals to that retrieved on the 2015 HST/STIS observation (Fig. 11), the closest available high resolution observation in time to these data and therefore our best estimate.

3.3 Brightening of the north polar hood from HST/WFC3 observations

We applied the IRW23 model to our HST/WFC3 dataset with the imaginary refractive index spectra and cloud-top CH₄ profile fixed to that retrieved from the 2015 HST/STIS observation at each latitude. We Minnaert-analysed the observations and, due to WFC3’s lack of spectral resolution, set the assumed errors to $\frac{1}{50}$ of the peak reflectivity within $0.1 \mu\text{m}$ wavelength bins, stepped by $0.05 \mu\text{m}$, across the wavelength range of each WFC3 filter (reflectivity values were taken from the disc-averaged 2015 HST/STIS observation to determine these errors). We used the Minnaert fits to generate reconstructed spectra at the two chosen zenith angles (0° , 61.45°). The scaling factor from Eqn. 2 was also implemented in an identical manner to capture the increase in uncertainty toward the extremities of the disc.

Retrievals were then carried out on the individual latitude bands using all seven WFC3 filters, with the free parameters in our aerosol model being the: aerosol-1 integrated opacity (τ_1), aerosol-2 integrated opacity (τ_2) & base pressure (p_2), and finally aerosol-3's integrated opacity (τ_3). All parameters were given 100% *a priori* errors. Spectral fits of the resulting retrievals at representative latitudes for the 2015 observations are shown in Fig. 12. Comparable fits were achieved for retrievals on the observations in each of the proceeding years.

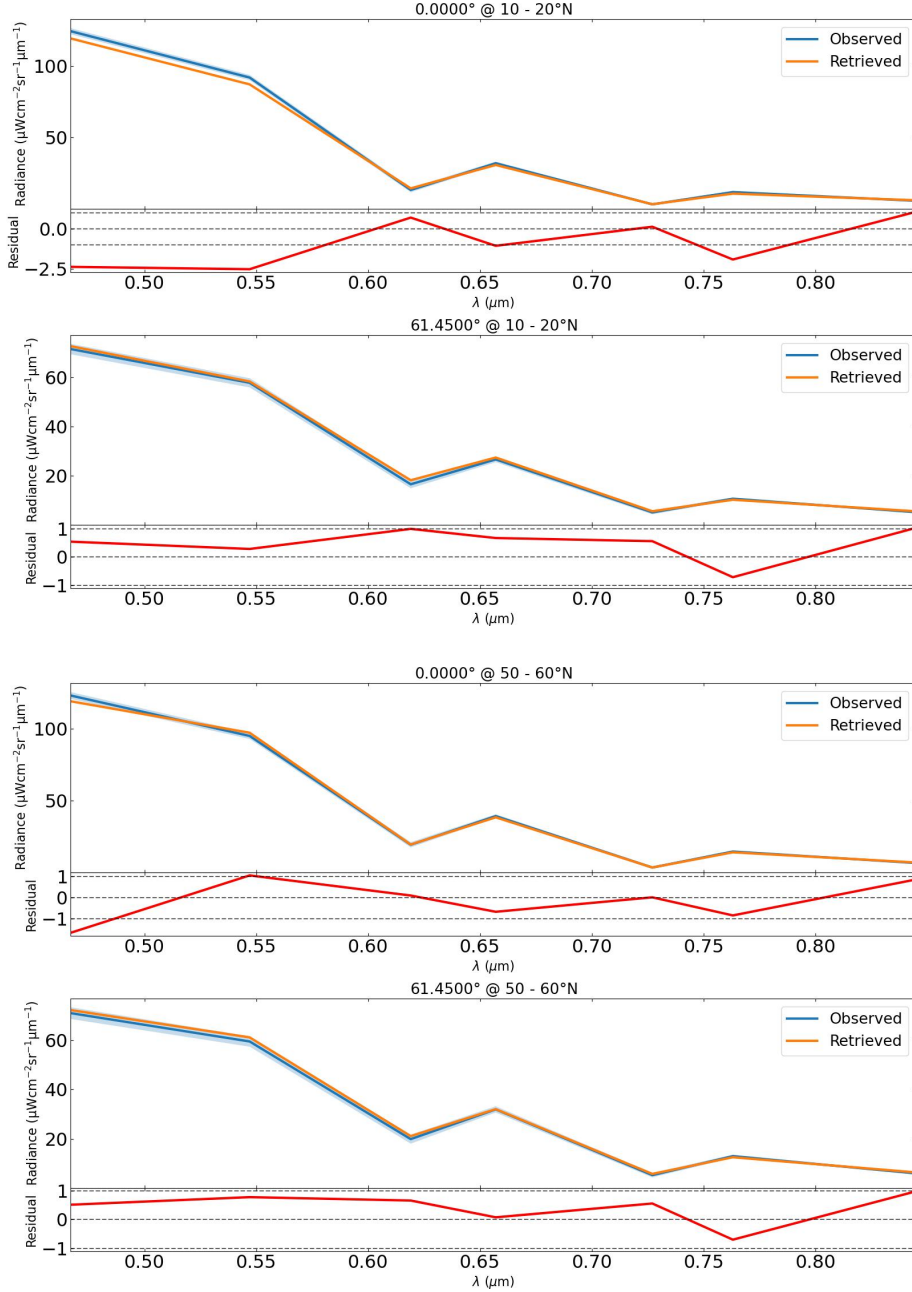


Figure 12. Spectral fits at the two chosen Minnaert zenith angles (0° , 61.45°) for retrievals carried out on the 2015 WFC3 observations at representative latitude bands of $10 - 20^\circ\text{N}$ (top) & $50 - 60^\circ\text{N}$ (bottom), with reduced- χ^2 values of ~ 1.53 and ~ 0.66 respectively. Note, residuals are divided by the error on the measured spectrum.

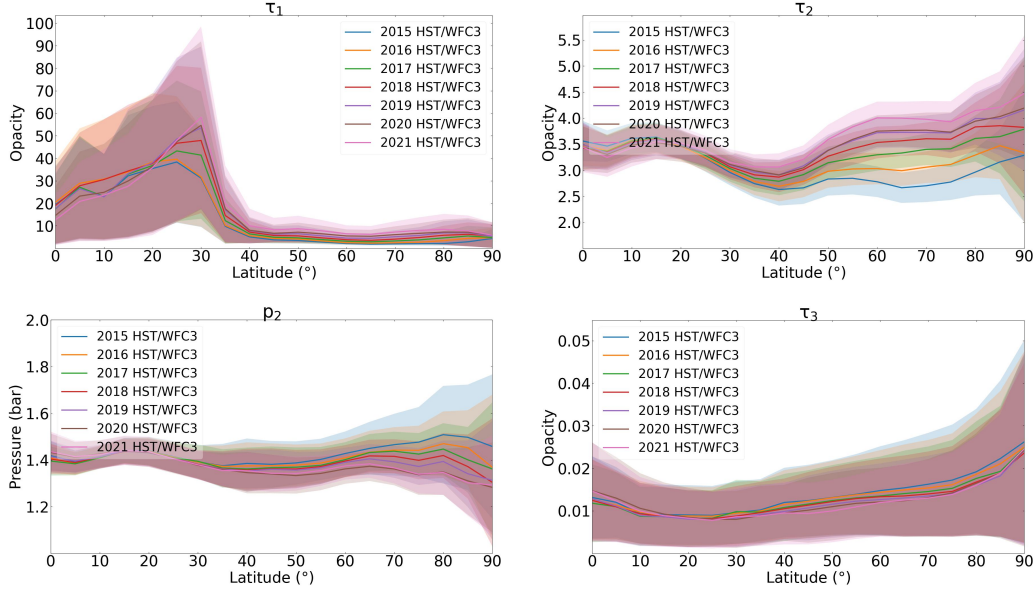


Figure 13. Latitudinal profiles in the northern hemisphere of the free parameters in the IRW23 vertical aerosol model retrieved from the entire HST/WFC3 dataset: aerosol-1 integrated opacity (τ_1), aerosol-2 base pressure (p_2) and integrated opacity (τ_2), and aerosol-3 integrated opacity (τ_3).

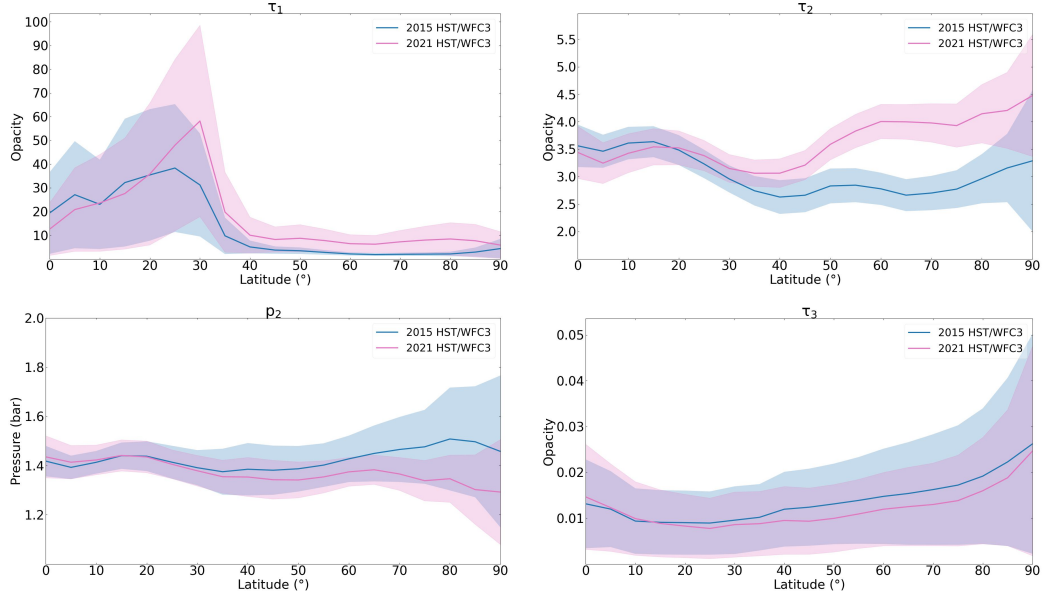


Figure 14. Latitudinal profiles in the northern hemisphere of the free parameters in the IRW23 vertical aerosol model retrieved from the 2015 & 2021 HST/WFC3 observations only: aerosol-1 integrated opacity (τ_1), aerosol-2 base pressure (p_2) and integrated opacity (τ_2), and aerosol-3 integrated opacity (τ_3). This plot demonstrates the overall change over the 6-year timespan of the dataset, showing an increase in τ_2 northwards of $\sim 45^\circ\text{N}$ as the only definitive change.

The retrieved latitudinal profiles of the free parameters were then plotted for the northern hemisphere to pinpoint the exact aerosol layer changes responsible for the polar hood brightening. The results are displayed for all years, and for the 2015 & 2021 datasets only, in Figs. 13 and 14 respectively. Our retrieval results clearly point to the integrated opacity of the 1 – 2 bar haze layer within the IRW23 model as the main culprit of the brightening, retrieving an average increase in the integrated opacity between 45 – 90°N from 2.9 ± 0.2 to 4.1 ± 0.2 , a 1.2 ± 0.3 increase at $0.8 \mu\text{m}$, between 2015 and 2021. All other retrieved profiles for the free parameters are consistent with no change across all northern latitudes over the entire timespan of the dataset. Note the sharp increase in τ_1 at $\sim 30^\circ\text{N}$ was a consistent feature in all of the retrievals carried out on this dataset.

The limited spectral resolution of the WFC3 instrument means that we are unable to reliably retrieve any change in the imaginary refractive index spectra of our aerosol layers with any confidence. As these spectra describe the optical properties of the aerosols, detailing the degree to which they are absorbing or reflecting for a given layer, this remains an important missing piece of the puzzle.

3.4 Further latitudinal analysis from HST/STIS

We sought to clarify whether or not an increase in τ_2 alone was sufficient to account for the spectral fingerprint of the polar hood brightening observed. This fingerprint is displayed in Fig. 15 in which an increase in radiance between the two polar spectra longwards of $\sim 0.6 \mu\text{m}$ is observed, with the brightening occurring predominantly at continuum wavelengths, suggesting that its main source originates from aerosol layer changes

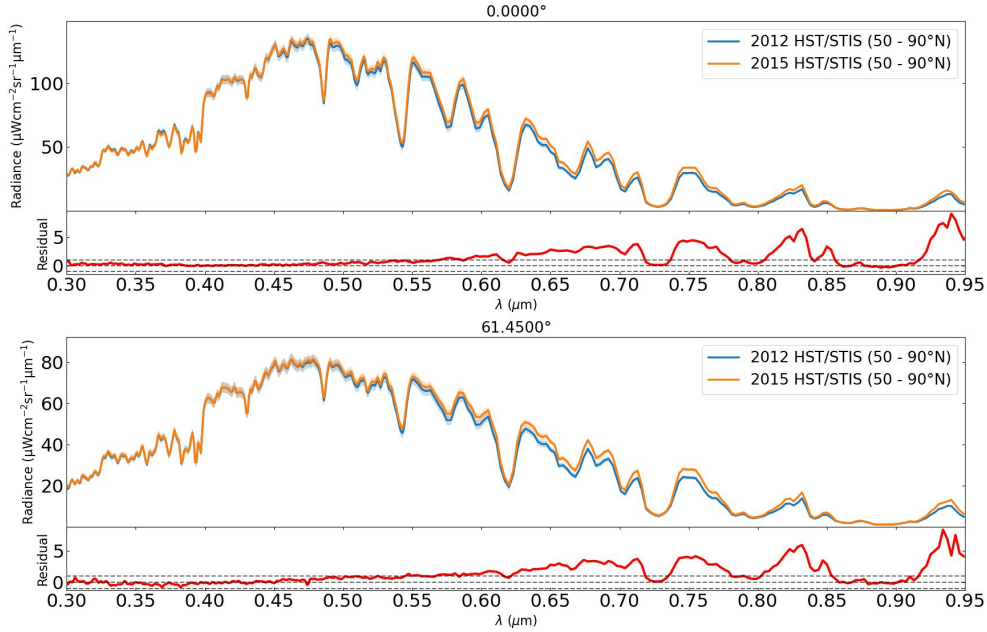


Figure 15. Plot of the 2012 & 2015 HST/STIS polar spectra extracted between 50°N and 90°N for our two chosen Minnaert zenith angles (0° , 61.45°). A clear increase in the radiance (i.e., a brightening) can be seen longwards of $\sim 0.6 \mu\text{m}$ between the two spectra. The residuals display the spectral fingerprint of this brightening. The brightening occurs predominantly at continuum wavelengths, suggesting that its main source originates from aerosol layer changes as opposed to changes in cloud-top CH_4 VMR. Note, residuals are divided by the error on the measured 2012 spectrum.

as opposed to changes in cloud-top CH_4 VMR (equatorial & mid-latitude spectra extracted between 0 - 40°N show no difference between the two observations within error). We employed a forward model approach with the NEMESIS retrieval code to carry out this analysis. In the scenario that an increase in τ_2 alone is not sufficient to match the observations, this approach affords the opportunity to narrow down additional parameters within our model that may be responsible for the observed brightening's spectral signature.

Upon running a forward model with an increase in τ_2 alone (see Fig. 16), it became evident that this scenario was very unlikely to be the full picture. Although this solution was able to reproduce a similar spectral brightening longwards of $\sim 0.6 \mu\text{m}$, it also produced a darkening at wavelengths short of $\sim 0.55 \mu\text{m}$. In light of the conclusions reached in Subsection 3.3, the simplest and most logical next step was to test changing the imaginary refractive index spectrum of aerosol-2 (n_{i2}), in addition to an increase in τ_2 . To counteract the short-wave darkening caused by the increase in τ_2 , the aerosol particles need to be more reflective (i.e., a decrease in n_{i2}). We therefore ran a forward model with a decrease in n_{i2} at all wavelengths and an increase in τ_2 , displayed in Fig. 17.

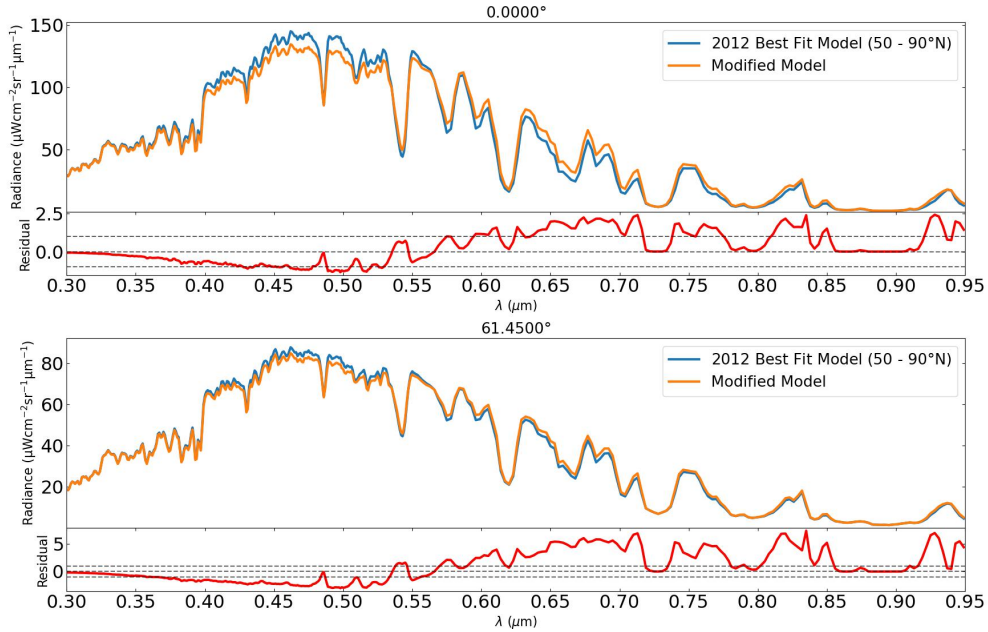


Figure 16. Plot comparing the retrieved spectrum of the IRW23 best-fit model at polar latitudes (50 – 90°N), carried out on the 2012 HST/STIS observation, to a forward model spectrum of a modified version of this model, testing an increase in the integrated opacity of aerosol-2 (τ_2). The residuals show a clear difference in profile from those of Fig. 15, suggesting that an increase in τ_2 alone is not sufficient to explain the nature of the observed polar hood brightening. Note, residuals are divided by the error on the best-fit model's measured spectrum.

This forward model matches the observed spectral fingerprint of the polar hood brightening fairly well. For completeness' sake, we tested forward models for all other combinations of parameters (including changes in the imaginary refractive index spectra of aerosol-1 and aerosol-3) involving an increase in τ_2 , as well as models without increasing τ_2 . The combination of increasing τ_2 and decreasing n_{i2} was the simplest model that matched the observations fairly well. Informed by this forward model study, latitudinal retrievals were then carried out in an identical manner to those in Subsection 3.2, but in this case, with n_{i2} the only imaginary refractive index spectrum free to vary.

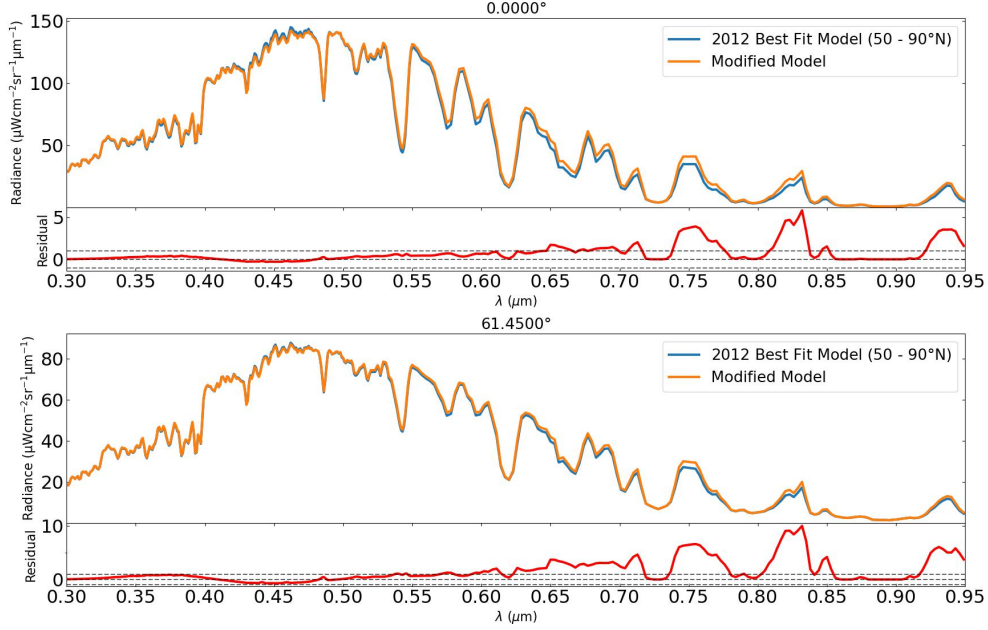


Figure 17. Plot comparing the retrieved spectrum of the IRW23 best-fit model at polar latitudes (50 – 90°N), carried out on the 2012 HST/STIS observation, to a forward model spectrum of a modified version of this model, testing an increase in the integrated opacity of aerosol-2 (τ_2) & a decrease at all wavelengths in the imaginary refractive index spectrum of aerosol-2. The residuals display a close resemblance to those from Fig. 15. Note, residuals are divided by the error on the best-fit model’s measured spectrum.

The results of these retrievals are projected onto synthetic discs of Uranus in Figs. 18 & 19, where the half-disc has been mirrored to create a full synthetic image of Uranus’ disc. The trends observed in τ_1 , τ_2 and cloud-top CH_4 VMR are consistent with strong subsidence in the polar domain in both the middle & upper tropospheres (Fletcher et al., 2020), resulting in the observed polar depletions (relative to the equatorial region). The τ_3 profile displays a concentration of haze in the equatorial region, suggesting a transport of haze from higher latitudes.

The results are also plotted in Figs. 20 to clearly display the differences between the retrieved profiles in the northern hemisphere between the two observations and Fig. 21 displays the retrieved imaginary index spectrum profiles at wavelength intervals of 0.1 μm . We see the same distinct increase in integrated opacity north of 45°N that we found from our WFC3 retrievals (see Fig. 14), here by an average of 1.09 ± 0.08 at 0.8 μm . We also see the same decrease in cloud-top CH_4 VMR as Fig. 11, here by an average of $0.19 \pm 0.03\%$ between 40°N – 80°N.

However, in addition to these changes noted from the aforementioned retrieval analyses of the HST/STIS & HST/WFC3 observations, we also see an increase in integrated opacity by an average of 0.6 ± 0.1 north of 45°N at 0.8 μm , incident with the polar hood. It should be noted that there is also a signal of increasing τ_1 south of the polar hood between $\sim 27 - 40^\circ\text{N}$. This could suggest an origin of the thickening stemming from south of the polar hood, or that the thickening is completely unrelated to the hood. We will comment on this further in the discussion in Section 4.

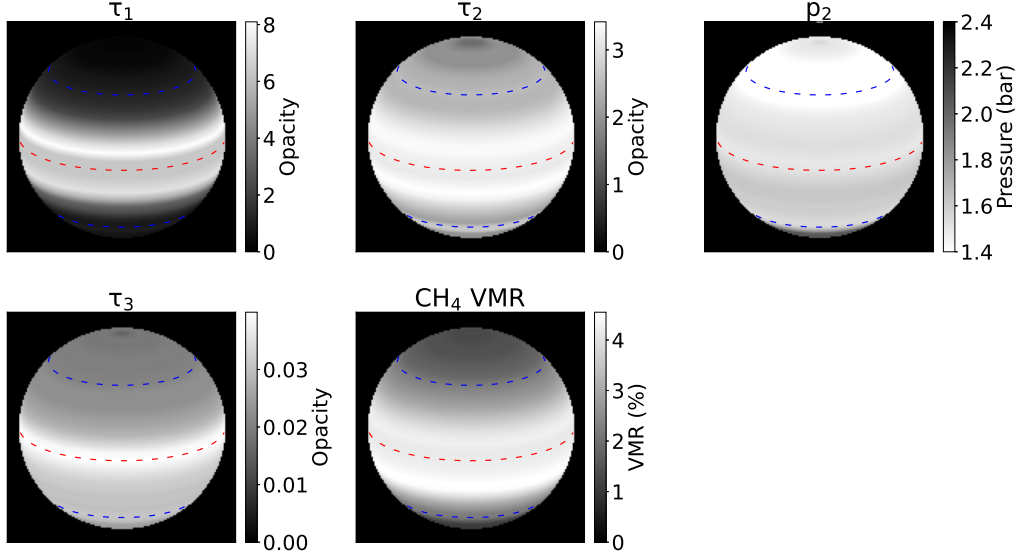


Figure 18. Synthetic images displaying the retrieved profiles of the free parameters (except the aerosol-2 imaginary refractive index spectrum shown in Fig. 21) within our 2012 HST/STIS retrievals: aerosol-1 integrated opacity (τ_1), aerosol-2 integrated opacity (τ_2) & pressure (p_2), aerosol-3 integrated opacity (τ_3), and cloud-top CH₄ VMR (labelled above each image). The north pole is located near to the top of the disc, with the red dashed line signifying the equator and the blue dashed lines signifying $\pm 45^\circ$. A comparison of the τ_2 image with the corresponding one in Fig. 19 reveals an increase in τ_2 in the north polar region. Note the sharp decrease in τ_2 at the pole is likely an artefact of the lack of constraint here.

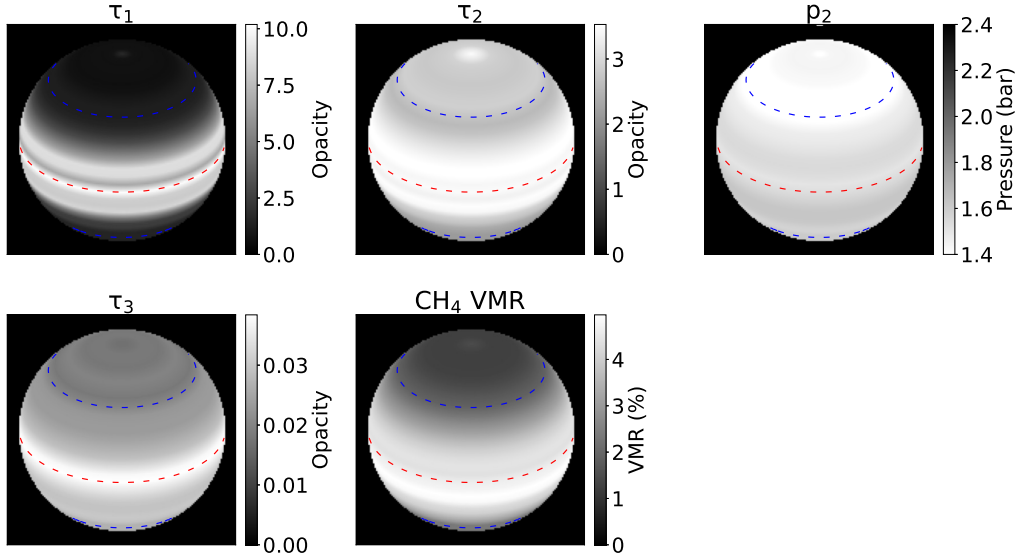


Figure 19. Similar to Fig. 21 but displaying retrieved profiles from the 2015 HST/STIS retrievals. Again, the aerosol-2 imaginary refractive index spectrum for these retrievals is shown in Fig. 21. Note the sharp increase in τ_2 at the pole is likely an artefact of the lack of constraint here.

Finally, the retrieved latitudinal profiles of aerosol-2's imaginary refractive index spectrum show a marked decrease between the 2012 and 2015 observations (Fig. 21) in the 0.7, 0.8, 0.9 & 1.0 μm channels north of $\sim 40^\circ\text{N}$, and between $60 - 80^\circ\text{N}$ at 0.5 μm , with the largest change mostly occurring at 60°N . This result denotes an increase in the scattering of the aerosols at these wavelengths, localised to the north polar hood (i.e., more reflective aerosols at polar hood latitudes within the 1 – 2 bar haze layer). No clear latitudinal trends in n_{i2} are observed at the four other, largely short-wave, wavelength channels (i.e., for 0.2, 0.3, 0.4 and 0.6 μm).

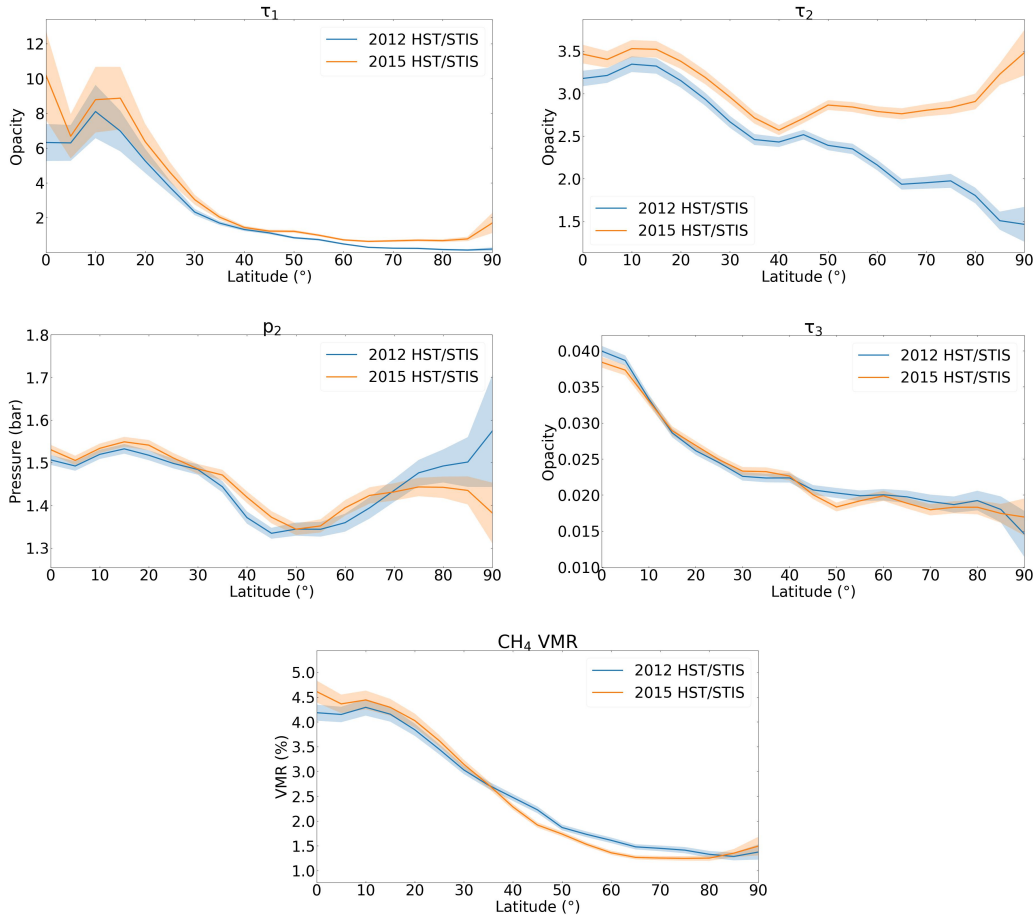


Figure 20. Retrieved latitudinal profiles of the free parameters (except the aerosol-2 imaginary refractive index spectrum shown in Fig. 21) within the IRW23 vertical aerosol model from our 2012 & 2015 HST/STIS retrievals: aerosol-1 integrated opacity (τ_1), aerosol-2 integrated opacity (τ_2) & pressure (p_2), aerosol-3 integrated opacity (τ_3), and cloud-top CH_4 VMR. A comparison of the two profiles reveals increases in τ_1 & τ_2 north of 45°N , as well as a decrease in the cloud-top CH_4 VMR between $\sim 40 - 80^\circ\text{N}$.

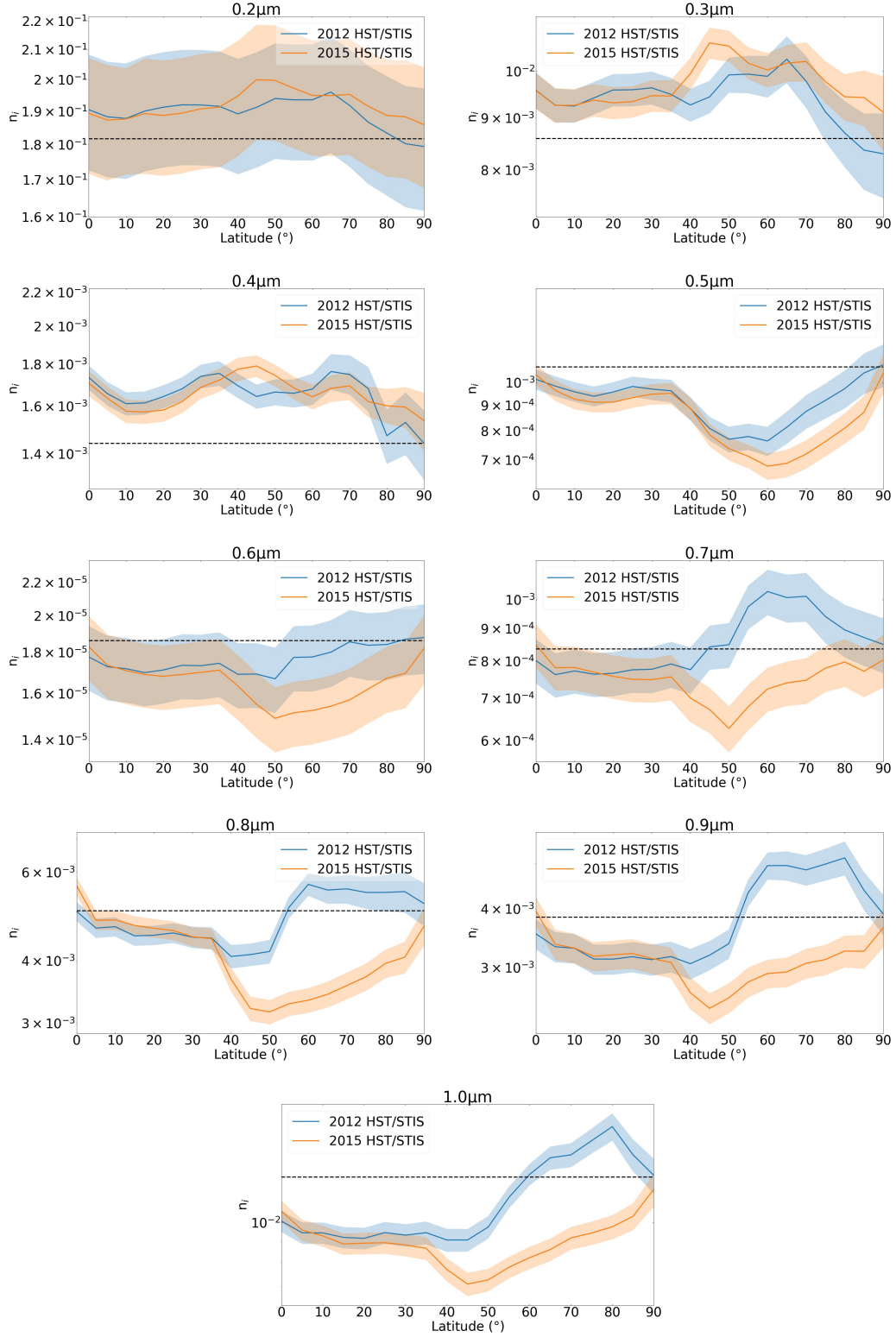


Figure 21. Retrieved latitudinal profiles of the aerosol-2 imaginary refractive index spectrum (n_{i2}) at each wavelength interval in the IRW23 vertical aerosol model from our 2012 & 2015 HST/STIS retrievals. A clear decrease in n_{i2} is observed north of $\sim 40^{\circ}\text{N}$ for wavelengths longwards of $\sim 0.7 \mu\text{m}$. A decrease in n_{i2} is also seen at $0.5 \mu\text{m}$ between $\sim 60 - 80^{\circ}\text{N}$. For the most part, the largest reduction occurs for the latitude band centred at 60°N . The black dashed lines represent the *a priori* values.

437 Alternatively, a comparison of the retrieved imaginary refractive index spectra for
 438 aerosol-2 at tropical and polar latitude bands is shown in Fig. 22, demonstrating the lat-
 439 itudinal variation across time.

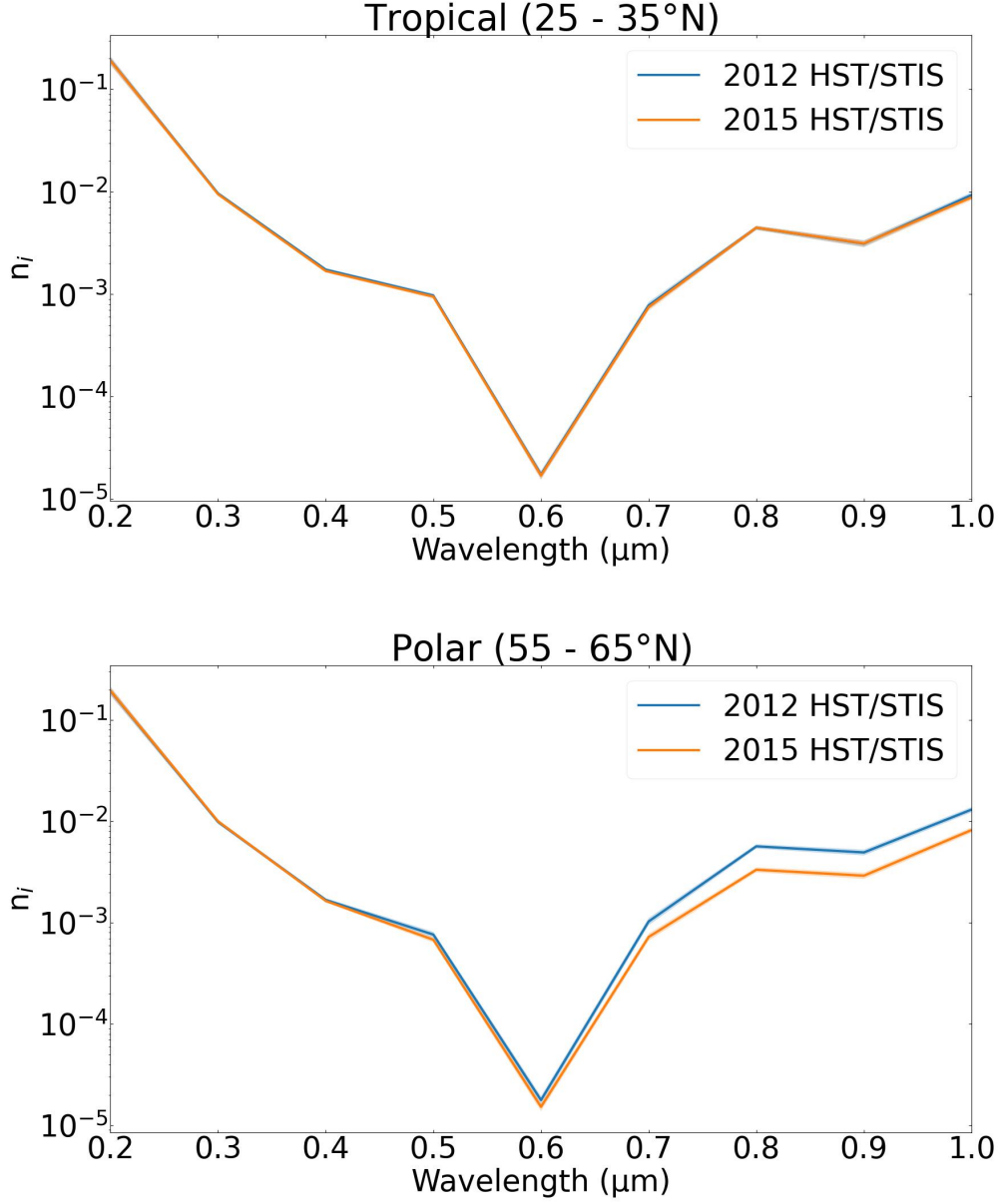


Figure 22. A comparison of the retrieved imaginary refractive index spectra (n_{i2}) for the aerosol-2 layer at representative tropical (25 – 35°N) and polar (55 – 65°N) latitudes from our 2012 & 2015 HST/STIS retrievals. A decrease in n_{i2} is observed across time here for wavelengths longwards of $\sim 0.6 \mu\text{m}$.

4 Discussion

4.1 Stability of the polar CH₄ depletion

As stated in Subsection 3.2, despite our retrievals showing a small decrease in the polar cloud-top CH₄ VMR at latitudes coincident with the polar hood, we settled on the conclusion of a ‘general stability’ in the polar depletion (Sromovsky et al., 2019) to be a safe, conservative one, given the limited window in time of the HST/STIS dataset. A third observation, obtained before Uranus reaches northern summer solstice in 2030, would enable this conclusion to be further put to the test. If future observations were to reveal a further decrease in cloud-top CH₄ VMR in the north polar region, this would support the trend returned by our retrievals, suggesting that some sort of dynamical change is occurring (likely a seasonal phenomenon linked to the orbital phase) that is driving a further depletion with time, calling into question its purported stability. One plausible candidate for this is a meridional circulation, previously presented as a potential mechanism to explain the existence of the polar depletion (e.g., Karkoschka and Tomasko (2009), Sromovsky et al. (2014), Fletcher et al. (2020)), that is changing over time. The proposed circulation leads to upwelling at equatorial latitudes and downwelling near the poles. This results in CH₄-rich gas from the lower troposphere rising up near the equator with CH₄ condensing out as it passes its condensation level ($\sim 1 - 2$ bar). This CH₄-poor gas is then transported polewards where it descends and likely suppresses convection from below the polar hood (Fletcher et al., 2020), leading to the observed upper tropospheric depletion in CH₄ (see Fig. 8 of Fletcher et al. (2020)).

A change in the meridional circulation presented above would likely be driven by the increasing insolation experienced by the northern hemisphere as the north pole shifts with time and points more directly towards the Sun as Uranus’ orbit progresses towards northern summer solstice. This could result in a slowing of the meridional circulation due to a heating of the north pole, resulting in a decrease in the rate of downwelling there. However, intuition tells us that this would lead to the opposite trend in cloud-top CH₄ VMR than we retrieved, namely an increase in polar cloud-top CH₄ VMR with time. This could hint at a more complex interplay between CH₄, aerosols and any potential meridional circulation. We will comment further on this in Subsection 4.2.

If future observations were to instead show an increase in cloud-top CH₄ compared to the retrieved profile produced by our retrievals on the 2015 HST/STIS observation, this would provide further support to the conclusion of a general stability within the polar depletion, hinting at interseasonal variability in the polar cloud-top CH₄ VMR over time.

In the scenario that the polar cloud-top CH₄ VMR is in fact decreasing with time, what would this mean for the retrieval results presented in this study? The only results relying on the assumption of stable CH₄ depletion are our HST/WFC3 retrievals probing latitudinal variation. The cloud-top CH₄ VMR for each latitude band was fixed to that retrieved from our 2015 HST/STIS observation. In theory, a further depletion of cloud-top CH₄, in line with the degree found from our HST/STIS retrievals (average decrease of $\sim 10\%$ between $45 - 90^\circ\text{N}$ between the 2012 & 2015 profiles), would account for a portion of the brightening attributed to the increase in the $1 - 2$ bar haze layer’s integrated opacity (τ_2). We would expect this to reduce the retrieved increase in τ_2 between the 2015 & 2021 HST/WFC3 observations. To put this prediction to the test, we re-ran our retrievals for the 2021 HST/WFC3 observations with a 20% reduction in cloud-top CH₄ VMR (in line with the degree of reduction retrieved between HST/STIS observations, i.e., 10% over 3 years) between $45 - 90^\circ\text{N}$. A comparison of the latitudinal profiles of τ_2 is shown in Fig. 23. All other retrieved profiles were omitted as they showed very little to no change within error, being practically identical to those seen in Fig. 14.

We see a relatively small reduction in τ_2 north of 45°N as predicted. We therefore assert with confidence that the question of stability in the polar cloud-top CH_4 depletion, in line with the degree of change observed from our HST/STIS retrievals with time, does not have a major bearing on the conclusions of our results.

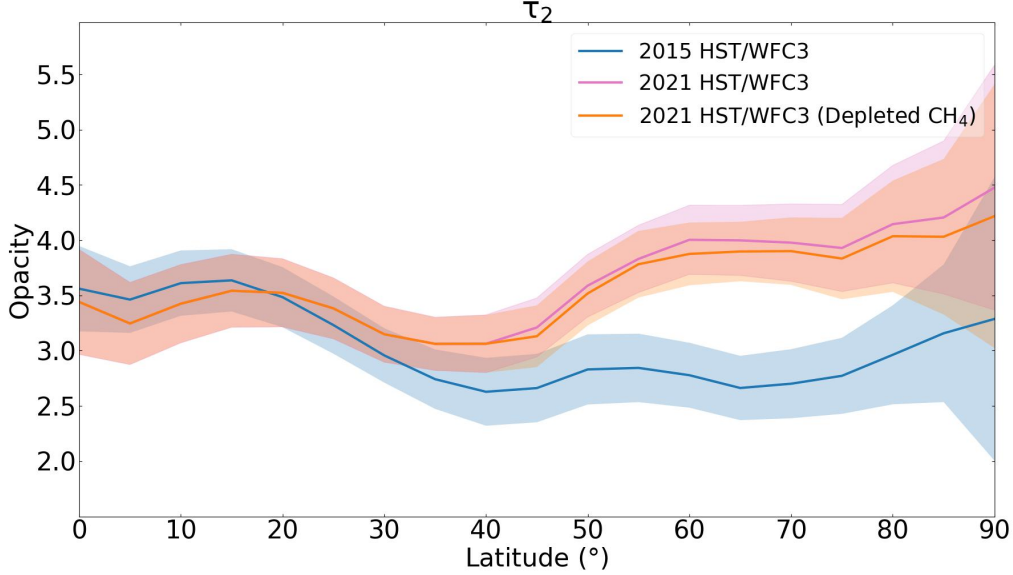


Figure 23. Plot of opacity against latitude displaying the retrieved latitudinal profiles of the integrated opacity of aerosol-2 (τ_2) produced from retrievals on the 2015 & 2021 HST/WFC3 observations. The orange line represents retrievals carried out on the 2021 observations in an identical manner to those of Section 3.3 but with the addition of a 20% reduction in cloud-top CH_4 (consistent with the average decrease with time found from our HST/STIS retrievals) between $45 - 90^\circ\text{N}$. A relatively small reduction in τ_2 north of 45°N can be seen as predicted.

4.2 Brightening of the north polar hood

Observations of Uranus’ polar hood over the past ~ 37 years, first in the southern polar region and, post-equinox, in the northern polar region, suggest that the hood is a seasonally-dependent phenomenon (i.e., linked to the orbital phase of the planet). The analysis and results presented in this paper are in alignment with this picture, leading us to a solution with which to explain the observed post-equinox brightening of this long-lived large-scale latitudinal feature.

Our initial HST/WFC3 Minnaert analysis confirmed an absolute brightening of the hood, ruling out any viewing geometry-related brightening effects. The observed depletion in cloud-top CH_4 VMR at polar latitudes Karkoschka and Tomasko (2009); Sromovsky et al. (2014, 2019), resulting in less absorption in the polar region, is one of the main contributors to the brighter appearance of the north polar hood when compared to equatorial latitudes Toledo et al. (2018). However, it was not entirely clear whether or not this depletion played a significant role in the observed brightening of the polar hood across time. As Uranus’ orbit progresses towards northern summer solstice in 2030, its north pole moves closer and closer to pointing directly towards the Sun, meaning that the path length of light incident on the hood is reduced, resulting in less and less CH_4 absorption with time for a fixed cloud-top CH_4 VMR. This would lead to an apparent brightening

over time at wavelengths of relatively weak CH₄ absorption. Sromovsky et al. (2019), analysing HST/STIS and near-infrared images from Keck’s Near Infrared Camera-2 (NIRC-2) instrument, refuted this as a significant source of the temporal brightening, finding wavelengths dominated by hydrogen absorption to also be increasing in brightness. In addition to our Minnaert analysis, we also found the spectral signature of the brightening to include wavelengths dominated by hydrogen absorption (818 - 832 nm) (see Fig. 18) in agreement with Sromovsky et al. (2019), leading us to the same conclusion that changes in the aerosol layers were the predominant cause of the brightening.

In light of this, within the framework of our vertical aerosol model (IRW23 model), we find that the 1 – 2 bar haze layer (aerosol-2 layer) is the main contributor to the observed brightening of the north polar hood over time via:

1. A thickening north of $\sim 45^\circ\text{N}$.
2. An increase in reflectivity of the aerosols north of 40°N and longwards of $\sim 0.7\ \mu\text{m}$, and also between $60 - 80^\circ\text{N}$ at $0.5\ \mu\text{m}$.

In addition to these changes, we see small contributions to the brightening stemming from an average reduction in cloud-top CH₄ VMR of $\sim 10\%$ north of $\sim 40^\circ\text{N}$, and a thickening of the deep aerosol-1 layer north of $\sim 45^\circ\text{N}$.

As noted in Subsection 3.4, the thickening of the aerosol-1 layer is not strictly localised to latitudes coinciding with the polar hood. There is a marked difference between the two regions of thickening established from our retrieval results. South of the polar hood between $\sim 27 - 40^\circ\text{N}$, the average increase in τ_1 retrieved for each latitude band is $\sim 20\%$, whereas for the thickening coincident with the hood (north of 45°N), the average increase is $\sim 56\%$, almost 3 times as great. It is not clear whether or not these two regions of thickening are linked, but we do see a trend of increasing integrated opacity as we move toward the pole, rising from a $\sim 23\%$ increase in the retrieved value at 30°N , to a $\sim 79\%$ increase at 90°N . It is plausible that this could be the result of a dynamical transport of haze polewards at the pressure level of aerosol-1 ($p \sim 4 - 7$ bar). It is noteworthy that these two regions of thickening are separated by a region of no change in the integrated opacity of aerosol-1. This region lies within the two latitude bands that simultaneously capture the boundary of the polar hood and the darker mid-latitudes (bands centred at 40°N & 45°N).

Fig. 24 displays a comparison between a forward model with a 56% increase in τ_1 compared to the baseline IRW23 model. We see that a thickening of the aerosol-1 layer, to the degree seen in our HST/STIS retrievals, does not result in much change at all in the spectrum, apart from two spikes in radiance (brightness) at the edge of the CH₄ absorption bands located at the long end of our wavelength range. When compared to the residuals in Fig. 18, we see that although this contribution is small, it is still significant (~ 2 sigma at 61.45°).

The combination of the HST/WFC3 and HST/STIS datasets resulted in an ideal complementary set of observations with which to carry out our analysis, providing both a wide temporal window and sufficient spectral resolution and coverage between the two datasets. It is important to note that with only two HST/STIS observations (i.e., only two snapshots in time), it is difficult to assert with a high degree of confidence that the parameters uniquely probed by these retrievals (i.e., cloud-top CH₄ VMR & n_{22}) reflect their trends over longer timescales. Further observations with comparable spectral resolution and spectral coverage are necessary to provide further context and support for our results.

Toledo et al. (2019)’s study constraining the structure, formation and transport of haze in Uranus’ atmosphere, via microphysical simulations, found that timescales for haze production are far too slow to account for the post-equinox rate of change in haze ob-

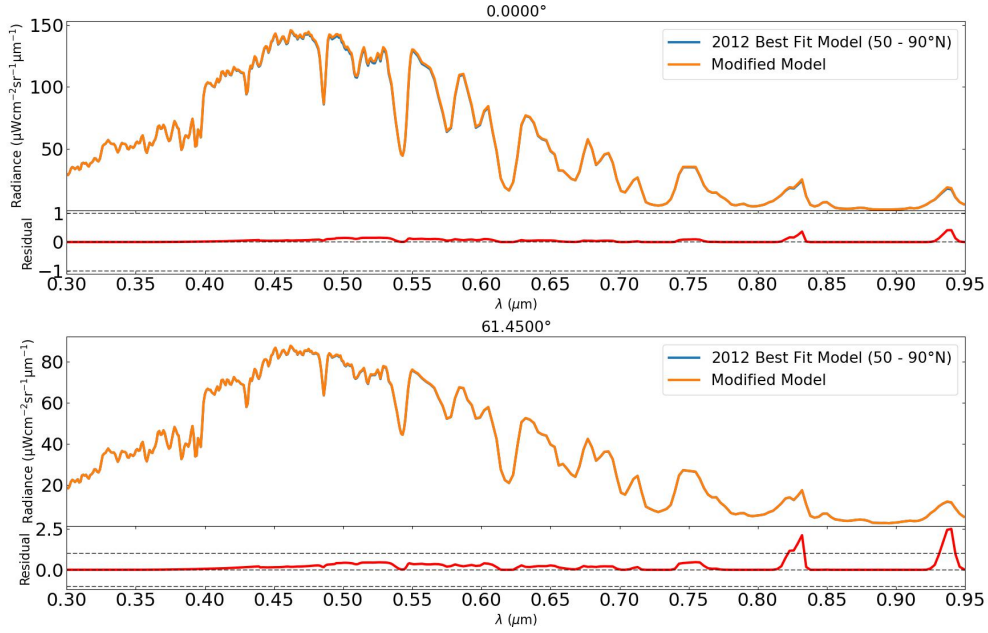


Figure 24. Plot comparing the retrieved spectrum of the IRW23 best-fit model at polar latitudes (50 – 90°N) carried out on the 2012 HST/STIS observation to a forward model spectrum of a modified version of this model, testing an increase in the integrated opacity of aerosol-1 (τ_1) only by 56%. We see from the residuals that there is only significant change to the spectrum at two small well-defined regions between 0.8 – 0.95 μm . Note, residuals are divided by the error on the best-fit model’s measured spectrum.

served in the northern hemisphere. With simulations returning timescales for haze particles to grow and settle out to be $\gtrsim 30$ years at pressure levels > 0.1 bar, Toledo et al. (2019) concluded that dynamics are likely the main factor controlling the spatial and temporal distribution of the haze over the poles. In addition to this, the observed changes through equinox are much faster than would be expected from radiative timescales (Conrath et al., 1990) and photochemical timescales (Moses et al., 2018). Toledo et al. (2019) put forward a meridional stratospheric transport of haze particles as a plausible explanation for the observed variations in haze structure. As mentioned earlier in Subsection 4.1, a meridional circulation has also been put forward in the literature to explain the observed polar depletion in cloud-top CH_4 VMR (e.g., Karkoschka and Tomasko (2009), Sromovsky et al. (2014), Fletcher et al. (2020)). One such circulation model is given by Fletcher et al. (2020) (see their Fig. 8), which takes into account findings from studies of Uranus’ zonal winds, latitudinal variations and stratospheric chemical tracers, amongst other considerations. This model consists of a number of vertically stacked circulation cells, including a stratospheric meridional circulation with upwelling at mid-latitudes and downwelling at the equator and poles. It is plausible that the thickening of the 1 – 2 bar haze layer that we find could be driven by such a circulation, with the transport of haze particles from equatorial regions to the mid-latitudes and onto the poles, where upon descent, they settle and accumulate at the 1 – 2 bar region of static stability (see Irwin et al. (2022) Fig. 23). It is important to note that although Fletcher et al. (2020)’s model is consistent with the findings from the observational studies considered in its construction, and despite it also being consistent with the trends observed in our Figs. 18 & 19, it is yet to be reproduced by global circulation models of Uranus’ atmosphere.

Returning to the discussion from Subsection 4.1, we speculated that as the season progresses and Uranus' northern hemisphere receives an increasing amount of insolation (i.e., increasing amounts of energy), this would result in a slowing of any meridional circulation that involves downwelling at the north pole via heating. This would be compounded by the fact that Uranus has a low internal source of heat (Pearl et al., 1990), providing relatively little energy to drive atmospheric dynamics from below, meaning any changes in solar flux are likely to have greater influence. In this scenario, a slowing in the rate of transport of haze would be expected, resulting in a reduction in the rate of thickening of the aerosol-2 haze within the polar hood. Analysing the average retrieved rate of change in τ_2 between consecutive years at polar hood latitudes ($45 - 90^\circ\text{N}$) resulted in no definitive trend being observed in the rate of brightening over time, but did not rule this out. In Subsection 3.1 we found a tentative decrease in the rate of polar hood brightening over the timespan of the HST/WFC3 dataset (see Fig. 7). Although these results are consistent with the slowing of a meridional circulation, we again reiterate that this model is speculative. Future work is certainly needed to shed more light on the circulation of the atmosphere of Uranus.

The 1 – 2 bar haze layer is coincident with pressures in which CH_4 is predicted to condense. Therefore, we expect the aerosols at 1 – 2 bar to act as cloud condensation nuclei (CCN), accumulating CH_4 ice as it condenses. This condensation results in an increase in mass of the aerosols as they accumulate more and more CH_4 , as well as a change in their optical properties (e.g., making them more absorbing or reflective at particular wavelengths). Unlike Neptune, Uranus' atmosphere does not seem to produce any stable, long-lasting CH_4 clouds (Irwin et al., 2017, 2022). One plausible explanation for the absence of CH_4 clouds predicts that as the aerosols accumulate CH_4 , they quickly reach a 'critical mass' and begin to sink, precipitating out of the 1 – 2 bar haze layer (Irwin et al., 2022). These precipitating CH_4 ice aerosols then sublime as they fall deeper into the atmosphere where temperatures are higher, releasing the photochemical haze particles that served as CCN, making them readily available to seed H_2S condensation in the 4 – 7 bar region (Irwin et al., 2022). We thus posit the question, what effect would a thickening of the aerosol-2 layer have on this proposed process?

CH_4 condensation is predicted to happen rapidly, with estimates of CH_4 ice particles at 1 – 2 bar in Ice Giant atmospheres growing to a size of ~ 5 μm in as little as $\sim 100\text{s}$ (Carlson et al., 1988). The thickening of the aerosol-2 layer with time (i.e., the accumulation of haze particles between 1 – 2 bar) within the polar hood would provide further CCN for CH_4 condensation. This could result in an increase in the number of particles precipitating out per unit of time, given a constant rate of accumulation of CH_4 , resulting in more haze particles being readily available below this level as CCN for H_2S condensation. This could explain the thickening of the aerosol-1 layer found from our HST/STIS retrievals. However, relaxing our assumption of a general stability in the polar cloud-top CH_4 VMR depletion, the retrieved decrease in polar cloud-top CH_4 would likely act to slow down the rate of accumulation of CH_4 onto the haze particles. This would result in the aerosols remaining within the 1 – 2 bar layer for a longer period before precipitation occurs. These longer-lasting aerosols would likely be smaller in size compared to at other latitudes, and could result in a change in the aerosol optical properties that matches the retrieved signature of a decrease in the imaginary refractive index spectrum (i.e., an increase in reflectivity of the aerosols). This is speculative as it is not currently known what the spectral identity of an increase in reflectivity of these aerosols would look like, and therefore how it would match up to the retrieved signature of an increase in reflectivity at ~ 0.5 μm and longwards of 0.7 μm . Work carried out by Mahjoub et al. (2012) on the influence of CH_4 concentration on the optical properties of Titan aerosol analogues does, however, provide plausibility to this speculative claim. They found that an increase in CH_4 concentration caused a decrease in the imaginary refractive index spectrum across the $0.37 - 1.0$ μm wavelength range for their aerosol analogues. A scenario in which the thickening of the aerosol-2 layer, combined with a decrease in polar cloud-

top CH₄ VMR, slows the rate of accumulation of CH₄ onto the haze particles, but to a degree whereby the number of aerosols precipitating out per unit of time is still increasing with time, could simultaneously explain the thickening of the aerosol-1 layer and the increase in reflectivity of the aerosol-2 particles.

5 Conclusions

We used observations of Uranus from the HST/WFC3 and HST/STIS instruments to analyse its north polar hood, a large-scale latitudinal atmospheric feature. The main objective was to narrow down the predominant cause of the hood's recent evolution (i.e., an apparent brightening). By combining complementary datasets, and adopting the IRW23 holistic vertical aerosol model, the work presented in this paper provides a solution using a retrieval and forward-model approach with the NEMESIS retrieval code. Our conclusions can be summarised as follows:

1. A Minnaert limb-darkening analysis of our HST/WFC3 dataset confirmed an absolute brightening of the polar hood, ruling out viewing geometry-related brightening effects as the main cause. We also observed a tentative reduction in the rate of polar hood brightening with time.
2. Retrievals on our HST/STIS supporting dataset revealed a further depletion in cloud-top CH₄ VMR, by an average of $0.19 \pm 0.03\%$ between 40°N and 80°N (i.e., a $\sim 10\%$ average reduction), between 2012 & 2015. However, due to unknown trends in the latitudinal cloud-top CH₄ profile over short and long timescales, we adopted a conservative approach, agreeing with the assertion of ‘general stability’ in the depletion posited by Sromovsky et al. (2019).
3. A combination of HST/WFC3 & HST/STIS latitudinal retrieval analyses found the main contributions responsible for the observed brightening of the polar hood to be, within the framework of the IRW23 vertical aerosol model:
 - a thickening of the aerosol-2 layer - finding an average increase in integrated opacity of 1.09 ± 0.08 north of $\sim 45^\circ\text{N}$ at $0.8 \mu\text{m}$.
 - an increase in reflectivity of the aerosol-2 particles north of $\sim 40^\circ\text{N}$ and longwards of $\sim 0.7 \mu\text{m}$, and also between 60°N and 80°N at $\sim 0.5 \mu\text{m}$.
4. From our HST/STIS retrievals, we also find small contributions to the polar brightening stemming from a thickening of the aerosol-1 layer, finding an average increase in integrated opacity of 0.6 ± 0.1 north of 45°N at $0.8 \mu\text{m}$ (i.e., a $\sim 56\%$ average increase) between 2012 and 2015, and from the aforementioned decrease in cloud-top CH₄ mixing ratio of $0.19 \pm 0.03\%$ between 40°N and 80°N ($\sim 10\%$ average decrease)
5. Our results are consistent with the slowing of a meridional circulation, similar to that posited by Fletcher et al. (2020), exhibiting downwelling at the poles.
6. Future observations with HST/STIS, or an instrument with comparable spectral resolution and coverage (e.g., the Very Large Telescope’s Multi Unit Spectroscopic Explorer), would enable more light to be shed on the question of the trend in the latitudinal distribution of cloud-top CH₄ over short and long timescales. These observations would either provide support for a further depletion in polar cloud-top CH₄ VMR with time, or an interseasonal variability in the VMR with time, supporting the picture of a general stability.

6 Open Research

The Uranus HST/STIS data used in this investigation are available on the MAST archive at <https://dx.doi.org/10.17909/T9KQ4N>.

All HST/WFC3 Uranus maps from the OPAL program are available at <http://dx.doi.org/10.17909/T9G593>, with the precise observations used in this investigation being available at <http://dx.doi.org/10.17909/det7-s122>.

The spectral fitting and retrievals were performed using the NEMESIS radiative transfer and retrieval algorithm Irwin et al. (2008) and is available to download at <https://doi.org/10.5281/zenodo.5816714>.

Acknowledgments

We are grateful to the United Kingdom Science and Technology Facilities Council for funding this research. STFC Student ID: J74250F.

This work used data acquired from the NASA/ESA HST Space Telescope, associated with OPAL program (PI: Simon, GO13937, with support provided to A. A. Simon, M. H. Wong, G. S. Orton, and T. K. Tsubota), and archived by the Space Telescope Science Institute, which is operated by the Association of Universities for Research in Astronomy, Inc., under NASA contract NAS 5-26555. Some of this research was carried out at the Jet Propulsion Laboratory, California Institute of Technology, under a contract with the National Aeronautics and Space Administration (80NM0018D0004).

L. N. Fletcher and M. T. Roman were supported by the European Research Council Consolidator Grant under the European Union’s Horizon 2020 research and innovation program (723890).

This work also used data acquired from the NASA/ESA HST Space Telescope, stored in the MAST archive by the Space Telescope Science Institute.

References

- Carlson, B. E., Rossow, W. B., & Orton, G. S. (1988). Cloud microphysics of the giant planets. *Journal of the Atmospheric Sciences*, *45*(14), 2066–2081. doi: 10.1175/1520-0469(1988)045<2066:CMOTGP>2.0.CO;2
- Conrath, B. J., Gierasch, P. J., & Leroy, S. S. (1990, feb). Temperature and circulation in the stratosphere of the outer planets. *Icarus*, *83*(2), 255–281. doi: 10.1016/0019-1035(90)90068-K
- Fletcher, L. N., de Pater, I., Orton, G. S., Hofstadter, M. D., Irwin, P. G., Roman, M. T., & Toledo, D. (2020). Ice Giant Circulation Patterns: Implications for Atmospheric Probes. *Space Science Reviews*, *216*(2), 1–38. Retrieved from <http://dx.doi.org/10.1007/s11214-020-00646-1> doi: 10.1007/s11214-020-00646-1
- Hammel, H. B., Sromovsky, L. A., Fry, P. M., Rages, K., Showalter, M., de Pater, I., ... Deng, X. (2009). The Dark Spot in the atmosphere of Uranus in 2006: Discovery, description, and dynamical simulations. *Icarus*, *201*(1), 257–271. Retrieved from <http://dx.doi.org/10.1016/j.icarus.2008.08.019> doi: 10.1016/j.icarus.2008.08.019
- Irwin, P. G. J., Dobinson, J., James, A., Toledo, D., Teanby, N. A., Fletcher, L. N., ... Pérez-Hoyos, S. (2021). Latitudinal variation of methane mole fraction above clouds in Neptune’s atmosphere from VLT/MUSE-NFM: Limb-darkening reanalysis. *Icarus*, *357*(December 2020). doi: 10.1016/j.icarus.2020.114277
- Irwin, P. G. J., Dobinson, J., James, A., Wong, M. H., Fletcher, L. N., Roman, M., ... Cook, S. L. (2023). Cloud Structure of Dark Spots and Storms in Neptune’s Atmosphere. *Accepted by Nature Astronomy*.
- Irwin, P. G. J., Teanby, N. A., & Davis, G. R. (2007). Latitudinal Variations in Uranus’ Vertical Cloud Structure from UKIRT UIST Observations. *The Astrophysical Journal*, *665*(1), L71–L74. doi: 10.1086/521189

- Irwin, P. G. J., Teanby, N. A., & Davis, G. R. (2009). Vertical cloud structure of Uranus from UKIRT/UIST observations and changes seen during Uranus' northern spring equinox from 2006 to 2008. *Icarus*, 203(1), 287–302. Retrieved from <http://dx.doi.org/10.1016/j.icarus.2009.05.003> doi: 10.1016/j.icarus.2009.05.003
- Irwin, P. G. J., Teanby, N. A., Davis, G. R., Fletcher, L. N., Orton, G. S., Calcutt, S. B., ... Hurley, J. (2012, mar). Further seasonal changes in Uranus' cloud structure observed by Gemini-North and UKIRT. *Icarus*, 218(1), 47–55. Retrieved from <https://doi.org/10.1016/j.icarus.2011.12.001> doi: 10.1016/J.ICARUS.2011.12.001
- Irwin, P. G. J., Teanby, N. A., Davis, G. R., Fletcher, L. N., Orton, G. S., Tice, D., & Kyffin, A. (2011). Uranus' cloud structure and seasonal variability from Gemini-North and UKIRT observations. *Icarus*, 212(1), 339–350. Retrieved from <http://dx.doi.org/10.1016/j.icarus.2010.12.018> doi: 10.1016/j.icarus.2010.12.018
- Irwin, P. G. J., Teanby, N. A., de Kok, R., Fletcher, L. N., Howett, C. J., Tsang, C. C., ... Parrish, P. D. (2008). The NEMESIS planetary atmosphere radiative transfer and retrieval tool. *Journal of Quantitative Spectroscopy and Radiative Transfer*. doi: 10.1016/j.jqsrt.2007.11.006
- Irwin, P. G. J., Teanby, N. A., Fletcher, L. N., Toledo, D., Orton, G. S., Wong, M. H., ... Dobinson, J. (2022). Hazy Blue Worlds: A Holistic Aerosol Model for Uranus and Neptune, Including Dark Spots. *Journal of Geophysical Research: Planets*, 127(6). doi: 10.1029/2022je007189
- Irwin, P. G. J., Wong, M. H., Simon, A. A., Orton, G. S., & Toledo, D. (2017). HST/WFC3 observations of Uranus' 2014 storm clouds and comparison with VLT/SINFONI and IRTF/Spex observations. *Icarus*, 288(2017), 99–119. doi: 10.1016/j.icarus.2017.01.031
- Karkoschka, E., & Tomasko, M. (2009). The haze and methane distributions on Uranus from HST-STIS spectroscopy. *Icarus*. doi: 10.1016/j.icarus.2009.02.010
- Karkoschka, E., & Tomasko, M. G. (2010). Methane absorption coefficients for the jovian planets from laboratory, Huygens, and HST data. *Icarus*, 205(2), 674–694. Retrieved from <http://dx.doi.org/10.1016/j.icarus.2009.07.044> doi: 10.1016/j.icarus.2009.07.044
- Mahjoub, A., Carrasco, N., Dahoo, P. R., Gautier, T., Szopa, C., & Cernogora, G. (2012). Influence of methane concentration on the optical indices of titan's aerosols analogues. *Icarus*, 221(2), 670–677. Retrieved from <http://dx.doi.org/10.1016/j.icarus.2012.08.015> doi: 10.1016/j.icarus.2012.08.015
- Minnaert, M. (1941). The reciprocity principle in lunar photometry. *The Astrophysical Journal*, 93(2), 403. doi: 10.1086/144279
- Moses, J. I., Fletcher, L. N., Greathouse, T. K., Orton, G. S., & Hue, V. (2018, jun). Seasonal stratospheric photochemistry on Uranus and Neptune. *Icarus*, 307, 124–145. doi: 10.1016/J.ICARUS.2018.02.004
- Pearl, J. C., Conrath, B. J., Hanel, R. A., Pirraglia, J. A., & Coustenis, A. (1990, mar). The albedo, effective temperature, and energy balance of Uranus, as determined from Voyager IRIS data. *Icarus*, 84(1), 12–28. doi: 10.1016/0019-1035(90)90155-3
- Pérez-Hoyos, S., Sánchez-Lavega, A., Sanz-Requena, J. F., Barrado-Izagirre, N., Carrión-González, O., Anguiano-Arteaga, A., ... Braude, A. S. (2020). Color and aerosol changes in Jupiter after a North Temperate Belt disturbance. *Icarus*, 352(August), 114031. Retrieved from <https://doi.org/10.1016/j.icarus.2020.114031> doi: 10.1016/j.icarus.2020.114031
- Sromovsky, L. A., & Fry, P. M. (2007). Spatially resolved cloud structure on Uranus: Implications of near-IR adaptive optics imaging. *Icarus*, 192(2), 527–557. doi:

10.1016/j.icarus.2007.07.017

Sromovsky, L. A., Fry, P. M., Hammel, H. B., Ahue, W. M., de Pater, I., Rages, K. A., ... van Dam, M. A. (2009). Uranus at equinox: Cloud morphology and dynamics. *Icarus*, 203(1), 265–286. Retrieved from <http://dx.doi.org/10.1016/j.icarus.2009.04.015> doi: 10.1016/j.icarus.2009.04.015

Sromovsky, L. A., Karkoschka, E., Fry, P. M., de Pater, I., & Hammel, H. B. (2019). The methane distribution and polar brightening on Uranus based on HST/STIS, Keck/NIRC2, and IRTF/SpeX observations through 2015. *Icarus*. doi: 10.1016/j.icarus.2018.06.026

Sromovsky, L. A., Karkoschka, E., Fry, P. M., Hammel, H. B., de Pater, I., & Rages, K. (2014). Methane depletion in both polar regions of Uranus inferred from HST/STIS and Keck/NIRC2 observations. *Icarus*. doi: 10.1016/j.icarus.2014.05.016

Toledo, D., Irwin, P. G., Rannou, P., Teanby, N. A., Simon, A. A., Wong, M. H., & Orton, G. S. (2019). Constraints on Uranus’s haze structure, formation and transport. *Icarus*. doi: 10.1016/j.icarus.2019.05.018

Toledo, D., Irwin, P. G., Teanby, N. A., Simon, A. A., Wong, M. H., & Orton, G. S. (2018). Uranus’s Northern Polar Cap in 2014. *Geophysical Research Letters*. doi: 10.1029/2018GL077654